A DENSITY FUNCTIONAL THEORY AND MANY BODY PERTURBATION THEORY BASED STUDY OF PHOTO-EXCITED CHARGE SEPARATION IN DOPED SILICON NANOWIRES WITH GOLD LEADS: TOY MODELS FOR THE PHOTOVOLTAIC EFFECT

A Thesis
Submitted to the Graduate Faculty
of the
North Dakota State University
of Agriculture and Applied Science

By

Nathan Thomas Walker

In Partial Fulfillment of the Requirements
for the Degree of
MASTER OF SCIENCE

Major Department:
Physics

April 2020

Fargo, North Dakota

NORTH DAKOTA STATE UNIVERSITY

Graduate School

Title

A DENSITY FUNCTIONAL THEORY AND MANY BODY PERTURBATION THEORY BASED STUDY OF PHOTO-EXCITED CHARGE SEPARATION IN DOPED SILICON NANOWIRES WITH GOLD LEADS: TOY MODELS FOR THE PHOTOVOLTAIC EFFECT

By

Nathan Thomas Walker

The supervisory committee certifies that this thesis complies with North Dakota State University's regulations and meets the accepted standards for the degree of

MASTER OF SCIENCE

SUPERVISORY COMMITTEE:

Professor Andrei Kryjevski
Chair

Professor Dmitri Kilin

Professor Svetlana Kilina

Professor Erik Hobbie

Approved:

April 17th, 2020
Date

Professor Sylvio May
Department Chair

ABSTRACT

We analyze a toy model for p-n junction photovoltaic devices by simulating photoexcited state dynamics in the atomistic models of silicon nanowires. One nanowire is approximately circular in cross section, with a diameter of $d = 11.7$ $\mathring{A}$. The other is approximately rhombic in cross section, with $d_1 = 11.6$ $\mathring{A}$ and $d_2 = 17.1$ $\mathring{A}$. Both nanowires have been doped with aluminum and phosphorus atoms and capped with gold leads. We use Boltzmann transport equation (BE) that includes phonon emission, carrier multiplication (CM), and exciton transfer. BE rates are computed using non-equilibrium finite-temperature many-body perturbation theory (MBPT) based on Density Functional Theory (DFT) simulations, including excitonic effects from Bethe-Salpeter Equation [1, 2]. We compute total charge transfer amount generated from the initial photoexcitation and find an enhancement when CM is included. In particular, we see between 78% and 79% enhancement in the smaller wire, while we see 116% enhancement in the larger nanowire.

ACKNOWLEDGEMENTS

I would like to acknowledge my advisor, Professor Andrei Kryjevski, and Professor Dmitri Kilin, for their guidance and contributions to this project. I would also like to thank Professor Erik Hobbie and Professor Svetlana Kilina for their input, and my fellow student Braden Weight for his insight. All computation was done on CCAST at NDSU.

DEDICATION

This thesis is dedicated to my family and the patience they have shown throughout the course of my education.

TABLE OF CONTENTS

ABSTRACT iii

ACKNOWLEDGEMENTS iv

DEDICATION v

LIST OF TABLES viii

LIST OF FIGURES ix

LIST OF APPENDIX FIGURES x

1. INTRODUCTION 1

1.1. Overview 1

1.2. Models 2

2. THE P-N JUNCTION 3

2.1. Overview 3

2.2. The Semi-Classical Model 4

2.3. The Equilibrium Case 4

2.4. The Photovoltaic Effect 7

3. METHODS 8

3.1. Density Functional Theory 8

3.1.1. The Born-Oppenheimer Approximation 8

3.1.2. Hartree-Fock Theory 10

3.1.3. Hohenberg and Kohn's First Theorem 11

3.1.4. Hohenberg and Kohn's Second Theorem 13

3.1.5. The Kohn-Sham Equations 14

3.1.6. HSE06 Hybrid Functional 15

3.2. Many Body Perturbation Theory 16

3.2.1. The Bethe-Salpeter Equation 16

3.2.2. Boltzmann Transport Equation 17

3.2.3. Electron-Phonon Coupling 17

3.2.4. MEG Rates 18

4. RESULTS 19

4.1. Density of States 19

4.2. Absorption 19

4.3. Impact Ionization Rates 21

4.4. Boltzmann Transport Equation and Charge Build-Up on the Leads in the Smaller Nanowire 21

4.5. Boltzmann Transport Equation and Charge Build-Up on the Leads in the Larger Nanowire 28

5. CONCLUSIONS AND OUTLOOK 32

REFERENCES 34

APPENDIX 40

LIST OF TABLES

Table Page

4.1. A table of charge enhancement for a variety of states corresponding to three peaks at 1.7 eV, 2.2 eV, and 2.45 eV for the smaller nanowire. 28

LIST OF FIGURES

Figure Page

1.1. **(a.)** circular nanowire with 282 atoms. $d = 11.7$ $\mathring{A}$. **(b.)** rhombic nanowire with 464 atoms.$d_1 = 11.6$ $\mathring{A}$ and $d_2 = 17.1$ $\mathring{A}$. 2

2.1. Graphical representation of the photovoltaic effect. 7

4.1. Phonon DOS for both nanowires, computed from VASP PBE Exchange-Correlation Functional. 20

4.2. Exciton and Bi-exciton DOS computed from the BSE for **(a.)** the smaller nanowire with $E_{gap} = 0.076$ eV, and **(b.)** the larger nanowire with $E_{gap} = 0.016$ eV. 20

4.3. Low-energy absorption spectra computed from BSE energies. 21

4.4. Impact Ionization Rate for **(a.)** the larger nanowire with $E_{gap} = 0.067$ eV and **(b.)** the thicker nanowire with $E_{gap} = 0.016$ eV. 22

4.5. Solutions to the BE for $n_\alpha(t)$ for the smaller nanowire, for the 14 lowest energy exciton states α. 22

4.6. Visualization of orbitals on the smaller nanowire for the four lowest exciton states **(a.)** $\alpha = 1$ **(b.)** $\alpha = 2$ **(c.)** $\alpha = 3$ **(d.)** $\alpha = 4$. 23

4.7. Orbitals for the excitons corresponding to absorption peaks at **(a.)** 1.7 eV, **(b.)** 2.2 eV, and **(c.)** 2.45 eV in the smaller nanowire. 25

4.8. Projected Density of States (PDOS) shows the contributions to each Kohn-Sham eigenvalue of each atom species for **(a.)** the smaller nanowire with a HOMO at -2.45 eV and **(b.)** the larger nanowire with a HOMO at -1.87 eV. 26

4.9. Plots of charge versus time in the smaller nanowire for initial excitations of **(a.)** 1.7 eV ($\alpha = 160$) **(b.)** 2.2 eV ($\alpha = 354$) **(c.)** 2.45 eV ($\alpha = 512$). 27

4.10. Orbitals of the exciton corresponding to an energy of 1.25 eV ($\alpha = 292$) in the thicker nanowire. 29

4.11. Solutions to the BE for $n_\alpha(t)$ for the thicker nanowire, for the 14 lowest energy exciton states α. 29

4.12. Visualization of orbitals on the larger nanowire for the states **(a.)** $\alpha = 1$ **(b.)** $\alpha = 2$ **(c.)** $\alpha = 3$ **(d.)** $\alpha = 4$. 30

4.13. A plot of charge versus time, both with and without MEG, for an excitation corresponding to 1.25 eV in the thicker nanowire. 31

LIST OF APPENDIX FIGURES

Figure Page

A.1. Solutions to the BE for intitial exciton excitations corresponding to the absorption peaks 1.7, 2.2, and 2.45 eV, corresponding to exciton states $\alpha = 165,\ 354,$ and 512, respectively. 40

1. INTRODUCTION

1.1. Overview

In p-n junction photovoltaic devices, solar range photons excite electrons into the conduction band, thus creating an electron-hole bound state (exciton). These excitons are then dissociated by the electric field inside the p-n junction to flow through the material as current [3]. Multiple Exciton Generation (MEG) is a process by which an exciton can decay into two lower energy excitons, thus increasing charge carriers in the system [4, 5, 6]. It is for this reason that MEG is also referred to as Carrier Multiplication (CM). However, a major competing process in the time evolution of a photoexcited state is known as phonon-mediated relaxtion, whereby an exciton decays into a lower energy exciton and a phonon [6]. While experiments have shown that in bulk materials, MEG is weak [7, 8, 9], it is expected to increase in nanoparticles due to quantum confinement [6, 10, 11, 12].

To model a p-n junction photovoltaic cell, we use a Si nanowire doped with Al and P, and capped with Au leads. In semiconductors such as Si, MEG is dominated by the impact ionization process [13, 14], so we therefore calculate the exciton-to-biexciton decay rate, the biexciton-to-exciton recombination rate, and exciton transfer whereby an exciton will "hop" across the system by decaying into an exciton of equal energy. It is the interplay of these processes that determine MEG [15, 16] so we use Many Body Perturbation Theory (MBPT) based on Density Functional Theory (DFT) calculations to calculate these rates and use the Boltzmann Transport Equation (BE) to simulate the time evolution of an excited state.

We perform geometrical optimization and calculate phonon frequencies using the Vienna Ab-Initio Simulation Package (VASP) [17, 18, 19, 20] in the plane wave basis, with the PBE [21] exchange-correlation functional and P.A.W. pseudo potentials, and Periodic Boundary Conditions (PBC). Kohn-Sham orbitals and energies are calculated with the HSE06 [22] hybrid functional, also in VASP, as a substitute for GW [23]. From the Kohn-Sham orbitals and energies we solve the Bethe-Salpeter Equation (BSE) [24] to include excitonic effects, and we calculate the aformentioned exciton-to-biexciton ($R_{1\to2}$) and biexciton-to-exciton ($R_{2\to1}$) decay rates, and the exciton-phonon rates. These rates are then plugged into the BE and allowed to 'compete.'

From the resultant occupancies we can calculate charge in the leads after some photoexcitation. Specifically, by calculating the charge in the leads both with and without MEG taken into account, we see an enhancement in charge that passes through the leads. By modeling two nanowires, each with a different width, we can test the effect of quantum confinement on MEG.

1.2. Models

In this work we simulate photoexcited state dynamics in two systems that constitute toy models of the p-n junction photovoltaic cell. Both systmes are (110) silicon nanowires that have been doped with 1 Al atom and 1 P atom each. In addition, both nanowires have been capped on either end with gold leads. Both are subject to PBC which results in a short circuit configuration in each case [25, 26]. One wire has a total of 282 atoms, and is approximately circular in cross section with a diameter of $d = 11.7$ $\mathring{A}$. The other nanowire has a total of 464 atoms, and is approximately rhombic in cross section with $d_1 = 11.6$ $\mathring{A}$ and $d_2 = 17.1$ $\mathring{A}$. Each model can be seen in Figure (1.1).

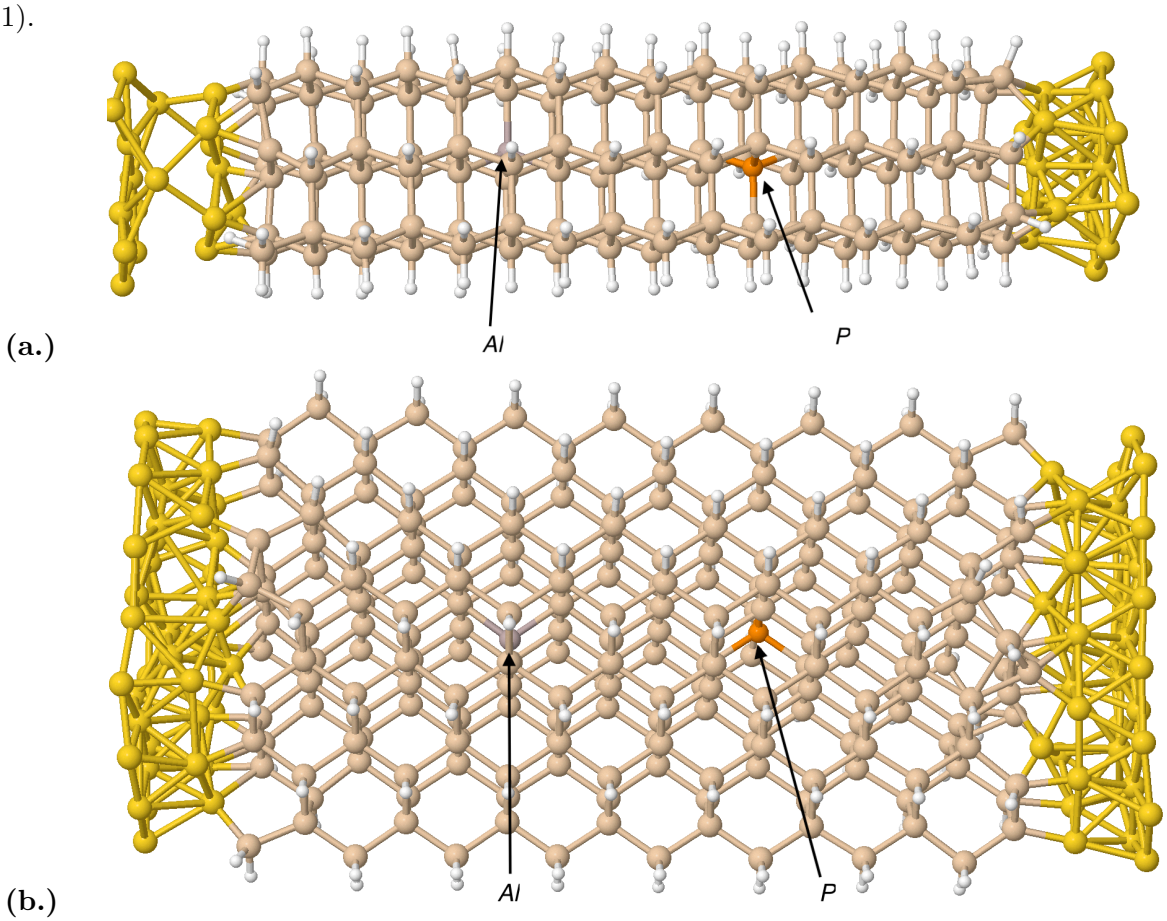

Figure 1.1. **(a.)** circular nanowire with 282 atoms. $d = 11.7$ $\mathring{A}$. **(b.)** rhombic nanowire with 464 atoms.$d_1 = 11.6$ $\mathring{A}$ and $d_2 = 17.1$ $\mathring{A}$.

2. THE P-N JUNCTION

2.1. Overview

A crucial component of understanding the evolution of charge separated states in a p-n junction photovoltaic device is of course the p-n junction itself, which creates an electric field that causes excitons in the semiconductor to separate into electrons and holes, and travel in opposite directions through the material. It is therefore the focus of this section to discuss the physics underlying the p-n junction. The derivations and definitions seen here follow those given by Ashcroft and Mermin [27].

P-n junctions belong to a class of semiconductors called inhomogeneous semiconductors , in which an intrinsic semiconductor, such as Si, has been doped with acceptor and/or donor impurity atoms such that the concentration of these atoms varies with position. The p-n junction is the case where the impurity concentration varies only in one direction, and only in a small spatial region. The so-called "doping profile" of the p-n junction is specified by the donor and acceptor densities, denoted $N_d(x)$ and $N_a(x)$, respectively. The density of electrons in the conduction band and the density of holes in the valence band will be denoted $n_c(x)$ and $n_v(x)$, respectively. It is important to note that we will only deal with "abrupt junctions," which are simply p-n junctions that can be described by doping profiles with a single discontinuous change, at $x = 0$:

$$N_d(x) = \begin{cases} N_d & x > 0 \\ 0 & x < 0 \end{cases} \quad , \quad N_a(x) = \begin{cases} 0 & x > 0 \\ N_a & x < 0 \end{cases} \tag{2.1}$$

In the following we will discuss the semiclassical model which forms the foundation of our treatment of the p-n junction, and we will discuss the carrier densities in the equilibrium case, as it is this case that is of most relevance to this work. Finally we will discuss the photovoltaic effect as it applies to p-n junctions.

2.2. The Semi-Classical Model

In the semiclassical model, we superimpose the potential due to the p-n junction on top of the the periodic potential of the lattice. Doing so, the Hamiltonian of the electrons in the n^{th} band is given by [28]

$$H_n = \varepsilon_n \left(\frac{\mathbf{p}}{\hbar}\right) - e\phi(x) \tag{2.2}$$

Here, the effects of the periodic lattice are contained in $\varepsilon_n \left(\frac{\mathbf{p}}{\hbar}\right)$. Given that we know the band energies of the periodic lattice of the intrinsic semiconductor (in our case, Si) and the potential $\phi(x)$ due to the impurity atoms (in our case Al and P), we can in principle calculate the band energies of the p-n junction. A limitation of this model is that it is only valid as long as $e\triangle\phi$ is small over a distance on the order of the lattice constant, when compared to the energy of the band gap.

2.3. The Equilibrium Case

In order to calculate $\phi(x)$ due to the impurity atoms, we need to calculate the density of charge carriers $n_c(x)$ and $n_v(x)$. To do this, we first consider the homogeneous case in thermal equilibrium at a temperature T. First, suppose we know the density of states for both the electrons in the conduction band, and the holes in the valence band. These will be denoted $g_c(\varepsilon)$ and $g_v(\varepsilon)$, respectively. Using Fermi-Dirac Statistics, we can find the density of carriers by integrating the density of states multiplied by the respective occupancies:

$$n_c(T) = \int_{\varepsilon_c}^{\infty} d\varepsilon g_c(\varepsilon) \frac{1}{e^{(\varepsilon-\mu)/k_B T}+1}, \tag{2.3}$$

$$p_v(T) = \int_{-}^{\varepsilon_v} d\varepsilon g_v(\varepsilon) \frac{1}{e^{(\mu-\varepsilon)/k_B T}+1}, \tag{2.4}$$

where for $p_v(T)$ we used the fact that $\langle p_v \rangle = 1 - \langle n_c \rangle$.

The next step is to make the assumption that we are dealing with a so-called nondegenerate semiconductor, in which case the following conditions hold:

$$\varepsilon_c - \mu >> k_B T, \qquad \mu - \varepsilon_v >> k_B T \tag{2.5}$$

Now, since in the conduction band every value for $\varepsilon > \varepsilon_c$, and in the conduction band every value for $\varepsilon < \varepsilon_v$, taken together with (2.5), the exponential terms in the denominators of both (2.3) and (2.4) are large, we can say:

$$\frac{1}{e^{(\varepsilon-\mu)/k_BT}+1} \approx e^{-(\varepsilon-\mu)/k_BT} \tag{2.6}$$

and

$$\frac{1}{e^{(\mu-\varepsilon)/k_BT}+1} \approx e^{-(\mu-\varepsilon)/k_BT} \tag{2.7}$$

These simplifications, taken with the following definitions:

$$N_c(T) = \int_{\varepsilon_c}^{\infty} d\varepsilon g_c(\varepsilon) e^{-(\varepsilon-\varepsilon_c)/k_BT} \tag{2.8}$$

$$P_v(T) = \int_{-\infty}^{\varepsilon_v} d\varepsilon g_v(\varepsilon) e^{-(\varepsilon_v-\varepsilon)/k_BT} \tag{2.9}$$

allow us to write:

$$n_c(T) = N_c(T) e^{-(\varepsilon_c-\mu)/k_BT} \tag{2.10}$$

$$p_v(T) = P_v(T) e^{-(\mu-\varepsilon_v)/k_BT} \tag{2.11}$$

To extend this to the inhomogeneous case, note that the Hamiltonian (2.2) takes the homogeneous energies, and shifts them by $-e\phi(x)$. Therefore, we can find the carrier densities in the inhomogeneous case, $n_c(x)$ and $p_v(x)$ by shifting the energies in (2.10) and (2.11) by $-e\phi(x)$ [29]

$$n_c(x) = N_c(T) e^{-(\varepsilon_c-e\phi(x)-\mu)/k_BT} \tag{2.12}$$

$$p_v(T) = P_v(T) e^{-(\mu-\varepsilon_v+e\phi(x))/k_BT} \tag{2.13}$$

Now we consider a special case where, far from the transition region at $x = 0$, the impurity atoms are fully ionized. Because of this the density of donor atoms is equal to the density of conduction band electrons, and the density of acceptor atoms equals the density of valence band holes. Mathematically:

$$N_d = n_c(\infty) = N_c(T)e^{-[\varepsilon_c - e\phi(\infty) - \mu]/k_B T} \tag{2.14}$$

$$N_a = p_v(-\infty) = P_v(T)e^{-[\mu - \varepsilon_v + e\phi(-\infty)]/k_B T} \tag{2.15}$$

Since μ in both (2.14) and (2.15) is the same, and (2.14) contains $\phi(\infty)$ while (2.15) contains $\phi(-\infty)$, we can combine both equations to find $\triangle\phi = \phi(\infty) - \phi(-\infty)$. This yields:

$$e\triangle\phi = E_g + k_B T \ln\left(\frac{N_d N_a}{N_c P_v}\right), \tag{2.16}$$

where $E_g = \varepsilon_c - \varepsilon_v$. We now have the potential difference across the p-n junction in terms of the density of acceptor and donor atoms from (2.1), and the integrals (2.8) and (2.9) at some temperature T.

It is sometimes convenient to define the so-called electrochemical potential:

$$\mu_e(x) = \mu - e\phi(x) \tag{2.17}$$

Now we can plug in values for $+\infty$ and $-\infty$ into (2.17) to rewrite (2.16) as:

$$e\triangle\phi = \mu_e(\infty) - \mu_e(-\infty) \tag{2.18}$$

Now that we have a boundary condition for $\phi(x)$, either of the form (2.16) or (2.18), we can start solving Poisson's Equation:

$$-\nabla^2\phi = -\frac{d^2\phi}{dx^2} = \frac{4\pi}{\epsilon}\rho(x), \tag{2.19}$$

where ϵ is the dielectric constant of the intrinsic semiconductor. Additionally, the simplification of $\nabla^2\phi = \frac{d^2\phi}{dx^2}$ can be made because the p-n junction only requires an x-dependence in ϕ and ρ. Here, $\rho(x)$ is the charge density that produces $\phi(x)$, and is made up of donor and acceptor atoms, as well as electrons and holes. Therefore, the charge density due to the added impurities is:

$$\rho(x) = e[N_d(x) - N_a(x) - n_c(x) + p_v(x)] \tag{2.20}$$

2.4. The Photovoltaic Effect

The Photovoltaic Effect can be seen in a device called a photodiode [3]. If light of an energy at least as big as the energy gap of the material falls on the diode, an electron will be excited into the conduction band, leaving behind a hole in the valence band. Electrons will then be swept in to the n-region of the p-n juntion, while holes will be swept into the p-region [3]. The current generated through this process must be extracted with metal diodes. In this work, we create a p-n junction by doping silicon nanowires with one Al atom and one P atom. The metal diodes are taken into account by capping the nanowires with Au clusters. See Figure (2.1) for an illustration of the photovoltaic effect.

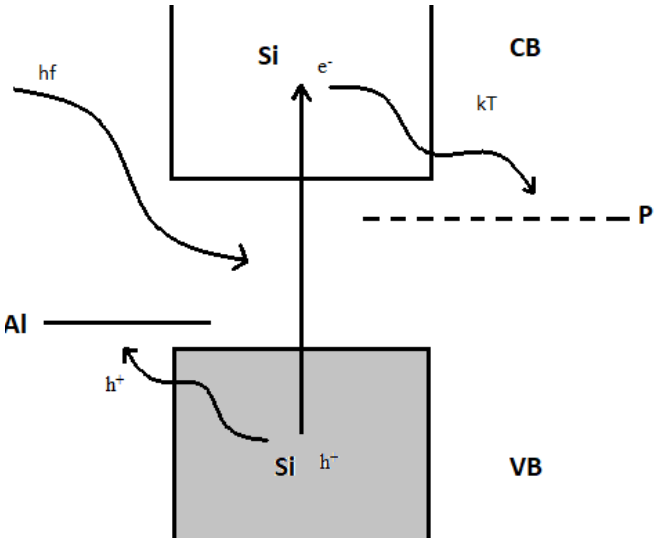

Figure 2.1. Graphical representation of the photovoltaic effect. A photon can excite an electron from the valence band (VB) into the conduction band (CB), leaving a hole behind in the VB. The electron can decay into the n-type region of the p-n junction (here a P atom), and the hole can be excited into the p-type region (here an Al atom). Thus current flows from the p-type region to the n-type region, consistent with an electric field that points from the n-type region to the p-type region.

3. METHODS

The methods used in this work are DFT as implemented in VASP, and MBPT (See [2]). We start with computing relaxed geometry and electronic structure in DFT, and from there use the DFT output to solve for rates of processes which require MBPT to describe. With those rates we solve the BE for state occupancies, which then allows us to calculate charge. This chapter will describe these methods and provide some theoretical background.

3.1. Density Functional Theory

Many aspects of this project rely on results from DFT simulations. The purpose of this section is to not only state the main equations used in DFT, but to also provide some background in terms of the approximations used in DFT, some theorems that prove the theory's validity, and on the related field of Hartree-Fock Theory.

3.1.1. The Born-Oppenheimer Approximation

While this work takes into account interactions that go beyond The Born-Oppenheimer Approximations (BO), it is nontheless an important starting point for DFT simulations. Stated simply, the BO (also referred to as the Adiabatic Approximation) assumes that the positions of the lighter electrons adjust adiabatically to the positions of the heavier nuclei [30]. Specifically, we separate the total molecular wavefunction Φ into a nuclear wavefunction that depends on the positions of the nuclei, and an electronic wavefunction that depends on the electronic positions as well as parametrically on the nuclear positions. Because of the critical nature of this approximation, the focus of this section will be to state it more formally.

To begin, we may write the Hamiltonian for a molecule or solid as

$$\hat{H} = \hat{H}_e + \hat{H}_N, \qquad \text{where} \tag{3.1}$$

$$\hat{H}_e = \sum_i \frac{-\hbar^2}{2m}\frac{\partial^2}{\partial \vec{r_i}^2} + V_{ee}(\vec{r}) + V_{eN}(\vec{r},\vec{R}), \qquad \text{and} \qquad \hat{H}_N = \sum_J \frac{-\hbar^2}{2M_J}\frac{\partial^2}{\partial \vec{R_J}^2} + V_{NN}(\vec{R}). \tag{3.2}$$

In (3.2), the sum over i goes over all electrons, and $\vec{r}_i$ refers to the position vector of the i^{th} electron. Likewise, the sum over J goes over all nuclei and $\vec{R}_J$ refers to the position vector of the J^{th} nuclei. The subscripts in the potential terms (denoted V) refer to whether the expressions describe the interaction between electrons (ee), nuclei (NN), or electrons and nuclei (eN). The variables $\vec{r}$ and $\vec{R}$ in the potential terms are understood to stand for the positions of all electrons and nuclei, respectively. With this in mind, it is clear that $\hat{H}_e$ contains all terms that depend in any way on the position of the electrons, and $\hat{H}_N$ refers to terms that depend *only* on the positions of the nuclei.

Now, we seek solutions to the Schrödinger equation for the molecular wavefunction: $\hat{H}\Phi = E\Phi$ as [31]

$$\Phi(\vec{r}, \vec{R}) = \psi_e(\vec{r}; \vec{R})\psi_N(\vec{R}). \tag{3.3}$$

ψ_N only has dependence on the positions of the nuclei and the semicolon in $\psi_e(\vec{r}; \vec{R})$ refers to the fact that we are assuming that the electronic wavefunction depends only on the positions of the nuclei as parameters. This is what is meant, mathematically speaking, when we say that lighter electrons adjust their positions adiabatically to the positions of the nuclei. The next step is to plug (3.2) and (3.3) into the Schrödinger Equation:

$$\begin{aligned}\psi_N(\vec{R}) \sum_i \frac{-\hbar^2}{2m} \frac{\partial^2}{\partial \vec{r}_i^2} \psi_e(\vec{r}; \vec{R}) + V_{ee}\psi_e\psi_N + V_{eN}\psi_e\psi_N + \sum_J \frac{-\hbar^2}{2M_J} \frac{\partial^2}{\partial \vec{R}_J^2} \Big(\psi_e(\vec{r}; \vec{R})\psi_N(\vec{R})\Big) \\ + V_{NN}\psi_e\psi_N = E\psi_e\psi_N.\end{aligned} \tag{3.4}$$

Expanding the second derivative in the sum over J,

$$\frac{\partial^2}{\partial \vec{R}_J^2} \Big(\psi_e(\vec{r}; \vec{R})\psi_N(\vec{R})\Big) = \psi_e \frac{\partial^2 \psi_N}{\partial \vec{R}_J^2} + \psi_N \frac{\partial^2 \psi_e}{\partial \vec{R}_J^2} + 2\frac{\partial \psi_e}{\partial \vec{R}_J} \frac{\partial \psi_N}{\partial \vec{R}_J}. \tag{3.5}$$

The BO consists of dropping the terms in this derivative that include derivatives of ψ_e with respect to $\vec{R}_J$ [31]. Doing so allows us to separate the Schrödinger Equation, yielding:

$$E = \epsilon_e(\vec{R}) + \epsilon_N \tag{3.6}$$

where E are the energy eigenvalues from the Schrödinger Equation.

3.1.2. Hartree-Fock Theory

While we use DFT instead of Hartree-Fock Theory (HFT) in this work, there are some shortcomings to exchange-correlation functionals used in DFT, and a partial application of HFT (so-called hybrid functionals) can be used to overcome these. In addition, there is some similarity to the procedure of the DFT and HFT, in that they are both self-consistent. It is therefore the purpose of this section to outline HFT.

We begin with the N-electron Schrödinger Equation (Here we assume the BO from the previous section): $\hat{H}\Psi = E\Psi$, where

$$\hat{H} = \sum_{i=1}^{n} \left(-\frac{\hbar^2}{2m}\nabla_i^2 - Ze^2 \sum_{\vec{R}} \frac{1}{\mid \vec{r}_i - \vec{R} \mid} \right) + \frac{e^2}{2} \sum_{i \neq j} \frac{1}{\mid \vec{r}_i - \vec{r}_j \mid}, \tag{3.7}$$

and Ψ is the N-electron ground state wavefunction. The Hamiltonian includes the kinetic energy of all the electrons, the attraction between electrons and the nuclei, and the repulsion between electrons. The goal from here is to find the ground state Ψ from the variational principle. We seek to minimize the energy $\left\langle \hat{H} \right\rangle$ in the state Ψ [32]:

$$\left\langle \hat{H} \right\rangle_{\Psi} = \frac{(\Psi, \hat{H}\Psi)}{(\Psi, \Psi)}, \qquad \text{where} \tag{3.8}$$

$$(\Psi, \Phi) = \sum_{s_1} \cdots \sum_{s_N} \int d\vec{r}_1 ... d\vec{r}_N \Psi^*(\vec{r}_1 s_1, ..., \vec{r}_N s_N) \Phi(\vec{r}_1 s_1, ..., \vec{r}_N s_N). \tag{3.9}$$

In order to minimize this energy, we will need an approximate form for Ψ. For that, we choose the Slater Determinant [32]:

$$\Psi(\vec{r}_1 s_1, ..., \vec{r}_N s_N) = \begin{vmatrix} \psi_1(\vec{r}_1 s_1) & . & . & . & \psi_1(\vec{r}_N s_N) \\ \psi_2(\vec{r}_1 s_1) & . & . & . & \psi_2(\vec{r}_N s_N) \\ . & & . & & . \\ . & & . & & . \\ \psi_N(\vec{r}_1 s_1) & . & . & . & \psi_N(\vec{r}_N s_N) \end{vmatrix} \tag{3.10}$$

Combining (3.8)-(3.10), it can be shown that [32]

$$\begin{aligned}\left\langle \hat{H} \right\rangle_{\Psi} =& \sum_i \int d\vec{r} \psi_i^*(\vec{r}) \left(-\frac{\hbar^2}{2m}\nabla^2 + U^{ion}(\vec{r}) \right) \psi_i(\vec{r}) \\ &+ \frac{1}{2}\sum_{i,j} \int d\vec{r} d\vec{r'} \frac{e^2}{\mid \vec{r} - \vec{r'} \mid} \mid \psi_i(\vec{r}) \mid^2 \mid \psi_j(\vec{r'}) \mid^2 \\ &- \frac{1}{2}\sum_{i,j} \int d\vec{r} d\vec{r'} \frac{e^2}{\mid \vec{r} - \vec{r'} \mid} \psi_i^*(\vec{r}) \psi_i(\vec{r'}) \psi_j^*(\vec{r'}) \psi_j(\vec{r}),\end{aligned} \tag{3.11}$$

where

$$U^{ion}(\vec{r}) = -Ze^2 \sum_{\vec{R}} \frac{1}{\mid \vec{r} - \vec{R} \mid}. \tag{3.12}$$

This suggests a single-electron Schrödinger equation of the form[32]:

$$\begin{aligned}-\frac{\hbar^2}{2m}\nabla^2\psi_i(\vec{r}) + U^{ion}(\vec{r})\psi_i(\vec{r}) + U^{el}(\vec{r})\psi_i(\vec{r}) \\ - \sum_j \int d\vec{r'} \frac{e^2}{\mid \vec{r} - \vec{r'} \mid} \psi_j^*(\vec{r'}) \psi_i(\vec{r'}) \psi_j(\vec{r}) \delta_{s_i s_j} = \varepsilon_i \psi_i(\vec{r}),\end{aligned} \tag{3.13}$$

where

$$U^{el}(\vec{r}) = -e \int d\vec{r'} \rho(\vec{r'}) \frac{1}{\mid \vec{r} - \vec{r'} \mid}. \tag{3.14}$$

The set of equations (3.13) for all N electrons are referred to as the Hartree-Fock Equations to be solved for $\psi_i(\vec{r})$, and one important feature is that they include the so-called exchange term, here denoted XC:

$$XC = -\sum_j \int d\vec{r'} \frac{e^2}{\mid \vec{r} - \vec{r'} \mid} \psi_j^*(\vec{r'}) \psi_i(\vec{r'}) \psi_j(\vec{r}) \delta_{s_i s_j} \tag{3.15}$$

3.1.3. Hohenberg and Kohn's First Theorem

As will be shown below, DFT depends on the fact it is possible to determine the effective potential appearing in the Kohn-Sham Equations uniquely from the electron charge density it induces. Here, we will state and prove the theorem which guarentees this, as prescribed by Hohenberg and Kohn.

Theorem **:** The ground state density $\rho(\vec{r})$ of a bound system of interacting electrons in some external potential $v(\vec{r})$ determines the potential uniquely. [33]

Proof : The Hamiltonian of a system of interacting electrons in some external potential can be written as:

$$\hat{H}_1 = v_1(\vec{r}) + T + V_{ee}, \tag{3.16}$$

where $v_1(\vec{r})$ is the external potential, T is the kinetic energy of the electrons, and V_{ee} is the electron-electron interaction. We can then write the ground state energy as

$$E_1 = \left\langle \psi_1 \mid \hat{H}_1 \mid \psi_1 \right\rangle = \int v_1(\vec{r})\rho(\vec{r})d\vec{r} + \langle \psi_1 \mid T + V_{ee} \mid \psi_1 \rangle \,, \tag{3.17}$$

where $\mid \psi_1\rangle$ is the ground state corresponding to the potential $v_1(\vec{r})$ and $\rho(\vec{r})$ is the ground state density. We can also consider another Hamiltonian with an effective potential $v_2(\vec{r})$, which produces the same ground state density:

$$\hat{H}_2 = v_2(\vec{r}) + T + V_{ee}. \tag{3.18}$$

This will have a ground state energy

$$E_2 = \left\langle \psi_2 \mid \hat{H}_2 \mid \psi_2 \right\rangle = \int v_2(\vec{r})\rho(\vec{r})d\vec{r} + \langle \psi_2 \mid T + V_{ee} \mid \psi_2 \rangle \,, \tag{3.19}$$

where $\mid \psi_2\rangle$ is the ground state corresponding to the potential $v_2(\vec{r})$.

From the Variational Principle, we know that $E_1 < \left\langle \psi_2 \mid \hat{H}_1 \mid \psi_2 \right\rangle$ and $E_2 < \left\langle \psi_1 \mid \hat{H}_2 \mid \psi_1 \right\rangle$. With this in mind, we can write

$$\begin{aligned} E_1 &< E_2 + \int v_1(\vec{r})\rho(\vec{r})d\vec{r} + E2 - \int v_2(\vec{r})\rho(\vec{r})d\vec{r}, \qquad \text{and} \\ E_2 &< E_1 + \int v_2(\vec{r})\rho(\vec{r})d\vec{r} + E1 - \int v_1(\vec{r})\rho(\vec{r})d\vec{r}, \end{aligned} \tag{3.20}$$

which is obtained by expanding the inner products and using (3.17) and (3.19) to solve for the terms with kinetic energy and the electron-electron interaction. Adding both equations in (2.20) yields

$$E_1 + E_2 < E_1 + E_2. \tag{3.21}$$

We have thus shown, via proof by contradiction, the validity of the first Hohenberg-Kohn Theorem.

3.1.4. Hohenberg and Kohn's Second Theorem

While the First Hohenberg-Kohn Theorem guarantees that we can uniquely determine the external potential from the charge density, we still need to be able to calculate ground state energy. That is the purpose of the Second Hohenberg-Kohn Theorem. As the name suggests, this was first shown by Hohenberg and Kohn, but here we will use a method devised by Jones. [34]

Theorem **:** Given a Hamiltonian of the form

$$\hat{H} = T + V_{ee} + v, \tag{3.22}$$

where v is the sum of all interactions v_{ext} with all N electrons, one can define [33] a universal functional as

$$F[\rho] = \langle \psi^{\rho}_{min} \mid T + V_{ee} \mid \psi^{\rho}_{min} \rangle \tag{3.23}$$

for some density ρ, and where the subscript min refers to the fact that the inner product is minimized. Given this functional, we can write the total energy as

$$E[\rho] \equiv \int d\vec{r} v_{ext}(\vec{r})\rho(\vec{r}) + F[\rho] \geq E_{GS}. \tag{3.24}$$

In particular, the ground state density determines the ground state energy:

$$E_{GS} = \int d\vec{r} v_{ext}(\vec{r})\rho_{GS}(\vec{r}) + F[\rho_{GS}]. \tag{3.25}$$

Proof **:** Since the charge density is equal to the modulus squared of the systems wave-function, we can write

$$\int d\vec{r} v_{ext}(\vec{r})\rho(\vec{r}) + F[\rho] = \langle \psi^{\rho}_{min} \mid v + T + V_{ee} \mid \psi^{\rho}_{min} \rangle \geq E_{GS}. \tag{3.26}$$

The inequality on the righthand side of (3.26) is because we know that E_{GS} is a minimum from the variational principle. Furthermore, we can combine (3.25) and (3.26) to get

$$E_{GS} = \langle \psi_{GS} \mid v + T + V_{ee} \mid \psi_{GS} \rangle \leq \langle \psi^{\rho_{GS}}_{min} \mid v + T + V_{ee} \mid \psi^{\rho_{GS}}_{min} \rangle . \tag{3.27}$$

Subtracting the v terms yields:

$$\langle \psi_{GS} \mid T + V_{ee} \mid \psi_{GS} \rangle \leq \langle \psi_{min}^{\rho_{GS}} \mid T + V_{ee} \mid \psi_{min}^{\rho_{GS}} \rangle \,, \tag{3.28}$$

and we know that the righthand side of (3.28) is minimized, so the equality must hold. Therefore,

$$\langle \psi_{GS} \mid T + V_{ee} \mid \psi_{GS} \rangle = \langle \psi_{min}^{\rho_{GS}} \mid T + V_{ee} \mid \psi_{min}^{\rho_{GS}} \rangle \tag{3.29}$$

We can therefore write

$$\begin{aligned} E_{GS} &= \int d\vec{r} v_{ext}(\vec{r}) \rho_{GS}(\vec{r}) + \langle \psi_{GS} \mid T + V_{ee} \mid \psi_{GS} \rangle \\ &= \int d\vec{r} v_{ext}(\vec{r}) \rho_{GS}(\vec{r}) + \left\langle \psi_{min}^{rho_{GS}} \mid T + V_{ee} \mid \psi_{mid}^{\rho_{GS}} \right\rangle \\ &= \int d\vec{r} v_{ext}(\vec{r}) \rho_{GS}(\vec{r}) + F[\rho_{GS}], \end{aligned} \tag{3.30}$$

thus proving that if we know the ground state density, we can calculate the ground state energy.

3.1.5. The Kohn-Sham Equations

We now present the self-consistent Kohn-Sham Equations that are used to determine the electronic structure of our systems. They are, without proof [35]:

$$\left(-\frac{\hbar^2}{2m} \nabla^2 + v(\vec{r}, [\rho(\vec{r})]) \right) \psi_i(\vec{r}) = \epsilon_i \psi_i(\vec{r}), \tag{3.31}$$

where $\psi_i(\vec{r})$ and ϵ_i are the so-called Kohn-Sham orbitals and energies respectively. Evidently, this resembles a system of single-electron Schrödinger Equations for some potential $v(\vec{r}, [\rho(\vec{r})])$, which is here defined, with square brackets denoting that it is a functional of density $\rho(\vec{r})$, as the functional derivative

$$v(\vec{r}, [\rho(\vec{r})]) = \frac{\delta(E^{tot}[\rho(\vec{r})] - T[\rho(\vec{r})])}{\delta \rho(\vec{r})}, \tag{3.32}$$

where $(E^{tot}[\rho(\vec{r})]$ is the total energy and $T[\rho(\vec{r})]$ is the kinetic energy. The density $\rho(\vec{r})$ can be constructed with:

$$\rho(\vec{r}) = \sum_i \mid \psi_i(\vec{r}) \mid^2 . \tag{3.33}$$

The procedure to solve these equations is to start with a given density, feed it into (3.31) to compute the Kohn-Sham Orbitals. With (3.33) we can then recalculate the density. This is repeated until there is s sufficiently small change in the density. Both this procedure, and the form of (3.31) are similar to the Hartree-Fock Equations (3.13). One critical difference is that (3.31) contains only approximation for the exchange term (3.15). To use (3.31), one must make a choice of density functional to account for different effects. In this work, we use the Perdew–Burke–Ernzerhof procedure (PBE-functional) [21] for geometry optimization, and the HSE06 Hybrid Functional [22] for electronic structure. We use HSE06 because it sometimes produces the correct energy gap due to its inclusion of the Hartree-Fock Exchange Term (3.15).

3.1.6. HSE06 Hybrid Functional

As mentioned above, the HSE06 Functional incorporates a part of the Hartree-Fock Exchange. What follows is taken from a seminal paper from Heyd et al. [22] and shows how HSE06 incorporates the Hartree-Fock Exchange term. We start with the PBE0 Hybrid Functional that is based on the PBE Exchange-Correlation Functional [21, 36, 37]:

$$E_{xc}^{PBE0} = aE_x^{HF} + (1-a)E_x^{PBE} + E_c^{PBE}, \tag{3.34}$$

where the subscripts x and c refer to wheter the terms are the exchange or correlation terms, respectively, and HF stands for Hartree-Fock. The constant a is known as the mixing coefficient, and is determined by perturbation theory ($a = 1/4$) [38]. Specifically, the exchange term is

$$E_x^{PBE0} = aE_x^{HF} + (1-a)E_x^{PBE}. \tag{3.35}$$

From here, the procedure is to break up each term into their short-range and long-range components:

$$\begin{aligned} E_x^{PBE0} =& aE_x^{HF,SR}(\omega) + aE_x^{HF,LR}(\omega) + (1-a)E_x^{PBE,SR}(\omega) \\ &+ E_x^{PBE,LR}(\omega) - aE_x^{PBE,LR}(\omega), \end{aligned} \tag{3.36}$$

where ω is an adjustable parameter which governs the strength of the short range interactions.

Based on numerical tests using realistic values of ω, the HF and PBE long range terms in equation (3.36) are small and tend to cancel each other. Noting this, the HF and PBE long range terms that are multiplied by a in equation (3.36) cancel. Adding back the PBE correlation term, we have

$$\begin{aligned} E_{xc}^{PBEh} =& aE_x^{HF,SR}(\omega) + (1-a)E_x^{PBE,SR}(\omega) \\ &+ E_x^{PBE,LR}(\omega) + E_c^{PBE}. \end{aligned} \tag{3.37}$$

Here we have a functional which incorporates the screened, short-range portion of the HF exchange term.

3.2. Many Body Perturbation Theory

Kohn Sham orbitals and energies are used as a convenient basis for MBPT calculations (See [2]). Therefore, once we have the results from DFT, we can start computing rates from MBPT. First, we must solve the BSE for exciton wavefunctions and energies. From there, the major competing processes we describe are MEG, phonon emission, and exciton transfer. With the results from the BSE we can compute the rates of each of these processes, and then use the BE to solve for occupancies. This section states the major equations used in each of these calculations.

3.2.1. The Bethe-Salpeter Equation

In this work we describe excited electrons as bound electron-hole pairs, which allows for an inclusion of excitons in the perturbative calculations to follow [39, 40, 41, 42]. To calculate the exciton wavefunctions and energies, we use the Bethe-Salpeter Equation(BSE) [43, 44], which in the static screening approximation is [24]

$$\begin{aligned} (\epsilon_{eh} - E^\alpha)\Psi_{eh}^\alpha + \sum_{e'h'}(K_{Coul} + K_{dir})(e,h;e',h')\Psi_{e',h'}^\alpha = 0, \\ K_{Coul} = \sum_{\vec{q}\neq 0} \frac{8\pi e^2 \rho_{eh}(\vec{q})\rho_{e'h'}^*(\vec{q})}{Vq^2}, \\ K_{dir} = -\frac{1}{V}\sum_{\vec{q}\neq 0} \frac{4\pi e^2 \rho_{ee'}(\vec{q})\rho_{hh'}^*(\vec{q})}{q^2 - \Pi(0,-\vec{q},\vec{q})}, \end{aligned} \tag{3.38}$$

where

$$\rho_{ji}(\vec{p}) = \sum_{\vec{k}} \phi_j^*(\vec{k}-\vec{p})\phi_i(\vec{k}) \tag{3.39}$$

is known as the transitional density, $\phi_j(\vec{p})$ are the momentum-space Kohn-Sham orbitals from (3.31), Ψ^{α}_{eh} are the exciton wavefunctions,

$$\Pi(\omega,\vec{k},\vec{p}) = \frac{8\pi e^2}{V\hbar}\sum_{ij}\rho_{ij}(\vec{k})\rho_{ji}(\vec{p})\left(\frac{\theta_{-j}\theta_i}{\omega-\omega_{ij}+i\gamma}-\frac{\theta_j\theta_{-i}}{\omega-\omega_{ij}-i\gamma}\right) \tag{3.40}$$

is the random phase approximation (RPA) polarization insertion [45], and

$$\hbar\omega_{ij}=\epsilon_{ij}, \sum_i \theta_i = \sum_{i>HO}, \sum_i \theta_{-i} = \sum_{i\leq HO} \tag{3.41}$$

Here, the Kohn-Sham orbitals in (3.39) are calculated using the Heyd-Scuseria-Ernzerhof (HSE06) exchange correlation functional [22].

3.2.2. Boltzmann Transport Equation

The time evolution of photoexcited states in nanoparticles includes dynames of electrons, phonons, and photons. In this work, we calculate the rates of various processes including electron-phonon couplling, exciton-to-biexciton rates, biexciton-to-exciton rates, and exciton transfer, and let them compete in the BE [2]. As shown in [2], the BE in the Kadanoff-Baym-Keldysh formalism for the slow time evolution of a photoexcited state is

$$\frac{dn_\alpha}{dt} = i\Sigma^{-+}_\alpha(n;\omega_\alpha)(1+n_\alpha) - i\Sigma^{+-}_\alpha(n;\omega_\alpha)n_\alpha, \qquad \omega_\alpha = \frac{E^\alpha}{\hbar}, \tag{3.42}$$

where Σ^{-+}_α and Σ^{+-}_α are the leading Keldysh exciton self-energies.

3.2.3. Electron-Phonon Coupling

To descripe phonon-mediated relaxation that includes one-phonon process, the BE is [2]

$$\frac{dn_\alpha}{dt} = \sum_{\alpha\mu}(G_1)^\mu_{\alpha\beta}(n_\beta n_\mu - n_\alpha(n_\beta+n_\mu+1))\delta(\omega_\alpha-\omega_\beta-\omega_\mu), \tag{3.43}$$

where

$$(G_1)^\mu_{\alpha\beta} \simeq \frac{2\pi}{\hbar^2}\left(\left|\sum_{ijk}\theta_{-i}\theta_j\theta_k g^\mu_{jk}(\Psi^\mu_{ji})^*\Psi^\beta_{ki}\right|^2 + \left|\sum_{ijk}\theta_i\theta_{-j}\theta_{-k}g^\mu_{jk}\Psi^\alpha_{ij}(\Psi^\beta_{ik})^*\right|^2\right), \tag{3.44}$$

$\delta(\omega_\alpha - \omega_\beta - \omega_\mu)$ is a finite-width delta function with a width parameter of $25meV$, and

$$g_{ij}^{\nu} = \sum_{I=1}^{N_i} \frac{4\pi i Z_I e^2}{V} \sqrt{\frac{\hbar}{2\omega_\nu M_I}} \sum_{\vec{p}} \frac{\rho_{ji}^*(\vec{p})\,(\vec{p}\cdot U_I^\nu)\,e^{-i\vec{p}\cdot\vec{R}_I}}{p^2 - \Pi(0,-\vec{p},\vec{p})} \tag{3.45}$$

are the electron-phonon couplings. In Equation (3.45), ω_ν are the normal phonon frequencies and $\vec{U}_l^\nu$ are the decompositional frequencies calculated from VASP [17, 18, 19, 20] in the plane wave basis, with the PBE [21] functional, respectively.

3.2.4. MEG Rates

To describe exciton-to-biexciton decay and biexciton-to-exciton recombination, the BE is [2]

$$\frac{dn_\alpha}{dt} = \sum_{\alpha\beta} R_{\alpha\beta}^{\gamma}(n_\alpha n_\beta - n_\gamma(n_\alpha + n_\beta + 1))\delta(\omega_\alpha + \omega_\beta - \omega_\gamma), \qquad \text{and} \tag{3.46}$$

$$n_\alpha \frac{dn_\beta}{dt} + n_\beta \frac{dn_\alpha}{dt} = -\sum_{\gamma} R_{\alpha\beta}^{\gamma}(n_\alpha n_\beta - n_\gamma(n_\alpha + n_\beta + 1))\delta(\omega_\alpha + \omega_\beta - \omega_\gamma), \tag{3.47}$$

where (3.46) describes impact ionization where an excition in state γ decays into excitons α and β. Equation (3.47) the process whereby these biexciton states decay back into a single exciton state. The rates $R_{\alpha\beta}^{\gamma}$ are [46]

$$\begin{aligned}
R_{\alpha\beta}^{\gamma} &= (R^p + R^h + \widetilde{R}^p + \widetilde{R}^h)\delta(\omega_\gamma - \omega_\alpha - \omega_\beta), \\
R^p &= \frac{4\pi}{\hbar^2}\left|\sum_{ijkln} W_{jlnk}\theta_l\theta_{-n}(\Psi_{ln}^{\beta})^*\theta_i\theta_{-j}\theta_{-k}\Psi_{ij}^{\gamma}(\Psi_{ik}^{\alpha})^*\right|^2 \\
R^h &= \frac{4\pi}{\hbar^2}\left|\sum_{ijkln} W_{jlnk}\theta_{-l}\theta_n\Psi_{nl}^{\beta}\theta_{-i}\theta_j\theta_k(\Psi_{ji}^{\gamma})^*\Psi_{ki}^{\alpha}\right|^2
\end{aligned} \tag{3.48}$$

where $\widetilde{R}^p$ and $\widetilde{R}^h$ take the same expressions for R^p and R^h and substitute W_{jlnk} with W_{jlkn}, and divide by 2. The terms W_{jlnk}, are defined as [2]

$$W_{jlnk} = \sum_{\vec{q}\neq 0} \frac{4\pi e^2}{V} \frac{\rho_{kj}^*(\vec{q})\rho_{ln}(\vec{q})}{(q^2 - \Pi(0,-\vec{q},\vec{q}))} \tag{3.49}$$

4. RESULTS

Using VASP [17, 18, 19, 20], we calculated electronic structure of two doped nanowire models of different sizes. Using results from VASP, we were able to compute phonon frequencies and exciton wavefunctions. From those, we computed density of states for both phonons and excitons, as well as the absorption spectra of each model. Additionally, we calculated the Impact Ioniziation Rates and solved the BE for time-dependant state occupancies. Finally, we computed charge build-up in the leads.

4.1. Density of States

Given the energies of phonons and excitons, we computed the density of states (DOS). The energies of phonons were computed using a Finite Difference Method [17] in VASP using ionic positions calculated with the PBE exchange-correlation functional. In the case of excitons, transitional densities computed from orbitals of an HSE06 hybrid-functional calculation in VASP were used to solve the BSE for exciton energies and wavefunctions. Using the exciton energies we computed plots of exciton and bi-exciton DOS. Plots of the phonon DOS for both nanowires are shown in Figure (4.1). The plots of exciton and bi-exciton DOS for both nanowires are shown in Figure (4.2).

In the case of the exciton DOS, there should be no density below the E_{gap}, and in the case of bi-exciton DOS there should be no density below $2E_{gap}$. In this case, the gap is small for both wires. Combined with the finite width of the delta function, we see some low energy densities. The gap of the larger nanowire is smaller than the gap of the smaller nanowire, and so we see lower energy densities with the thicker nanowire compared to the smaller nanowire. However, in both nanowires the bi-exciton DOS is shifted to the right relative to the exciton DOS, which is to be expected.

4.2. Absorption

Figure (4.3) shows the absorption spectra of both nanowires overlaid on each other, and select peaks are highlighted. Using the absorption spectrum of a given model, we can target specific energies that are absorbed and run excited state dynamics for the states corresponding to those

peaks. For the smaller nanowire we highlight $1.7eV$ and $2.45eV$, and for the larger nanowire we highlight $0.65eV$ and $1.9eV$.

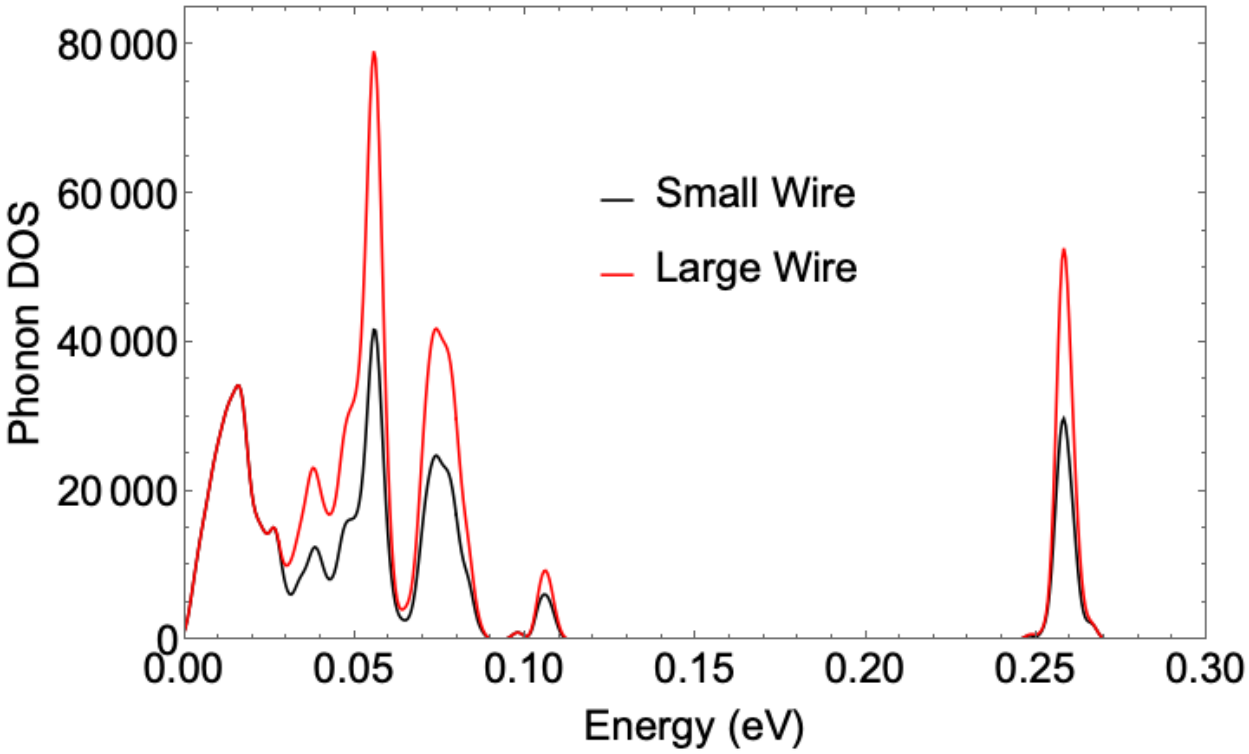

Figure 4.1. Phonon DOS for both nanowires, computed from VASP PBE Exchange-Correlation Functional.

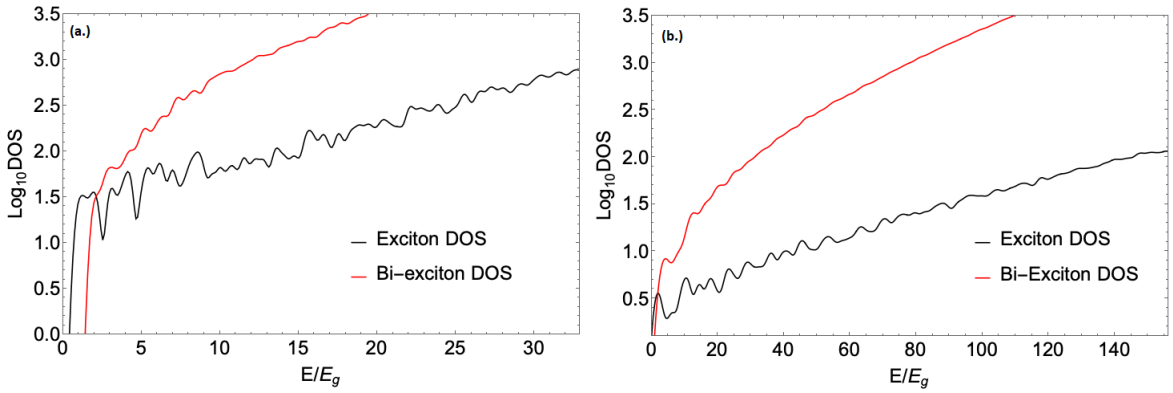

Figure 4.2. Exciton and Bi-exciton DOS computed from the BSE for **(a.)** the smaller nanowire with $E_{gap} = 0.076\ eV$, and **(b.)** the larger nanowire with $E_{gap} = 0.016\ eV$. Both plots are on a log scale.

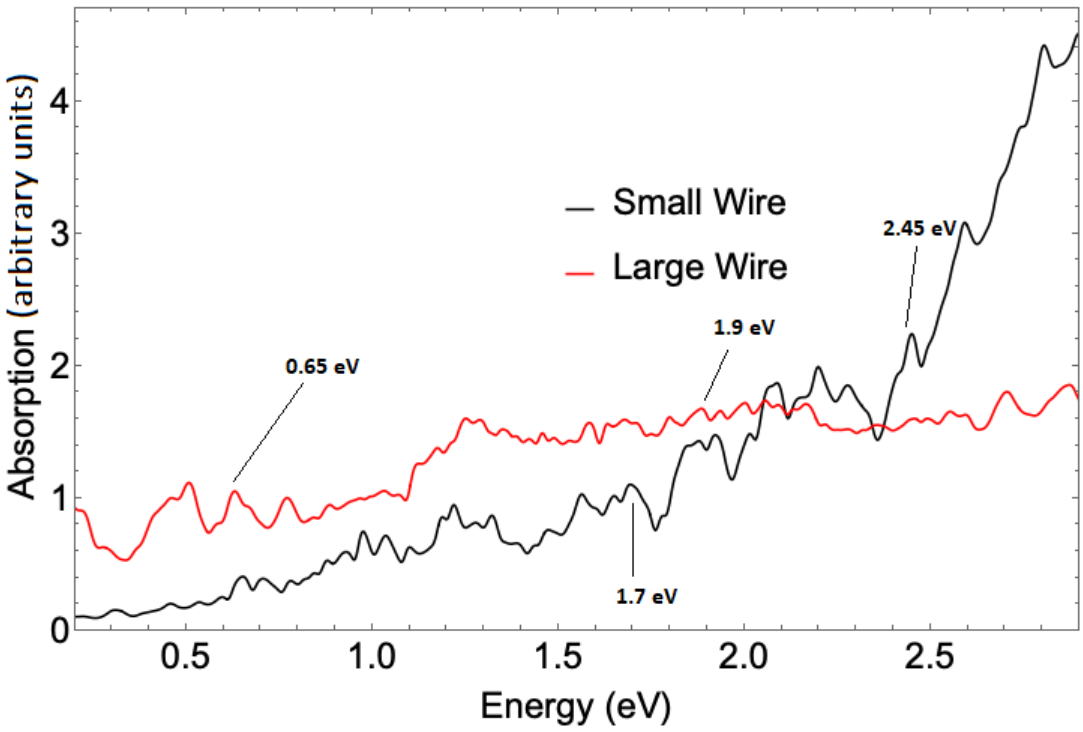

Figure 4.3. Low-energy absorption spectra computed from BSE energies. Apsorption peaks are highlighted at 1.7 eV and 2.45 eV for the smaller nanowire, and 0.65 eV and 1.9 eV for the larger nanowire.

4.3. Impact Ionization Rates

From the results of the BSE and transitional densities, we calculated the Impact Ionization Rate [2], shown in Figure (4.4). Normally it would be expected that $R_{1\to 2} = 0$ for $E < 2E_{gap}$. In this case, a combination of a small gap and finite width lead to non-zero rates below $2E_{gap}$. However, in both cases there is a trend for $R_{1\to 2}$ to approach zero as $E_{gap} \to 0$.

4.4. Boltzmann Transport Equation and Charge Build-Up on the Leads in the Smaller Nanowire

Using MEG rates, rates from one-phonon coupling processes, and exciton transfer, we can solve the BE for state occupancies. Figure (4.5) shows solutions for the first 14 lowest energy states. There is a mix of transient states, where occupied states decay relatively quickly into unoccupied states; and states that remain occupied. The states which remain unoccupied are localized on the leads, as can be seen in Figure (4.6).

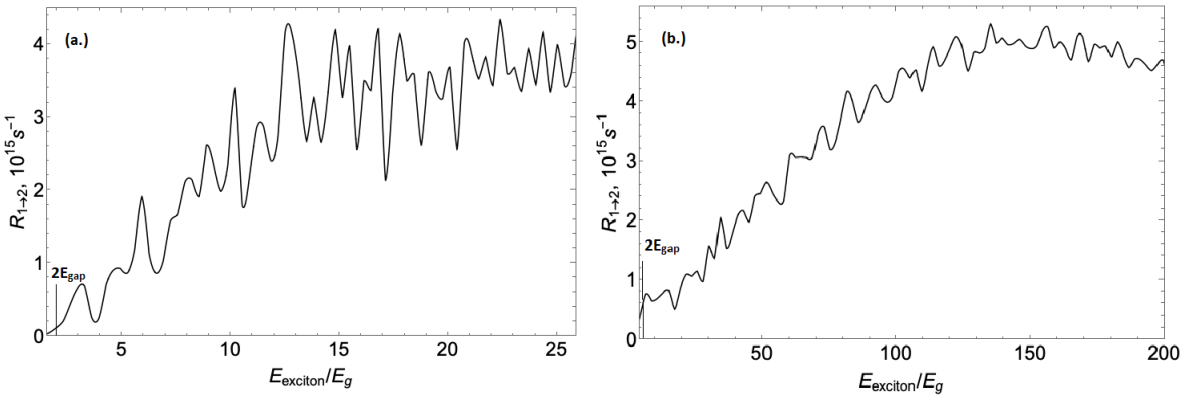

Figure 4.4. Impact Ionization Rate for **(a.)** the larger nanowire with $E_{gap} = 0.067\ eV$ and **(b.)** the thicker nanowire with $E_{gap} = 0.016\ eV$. Labeled on both plots are the locations of $2E_{gap}$.

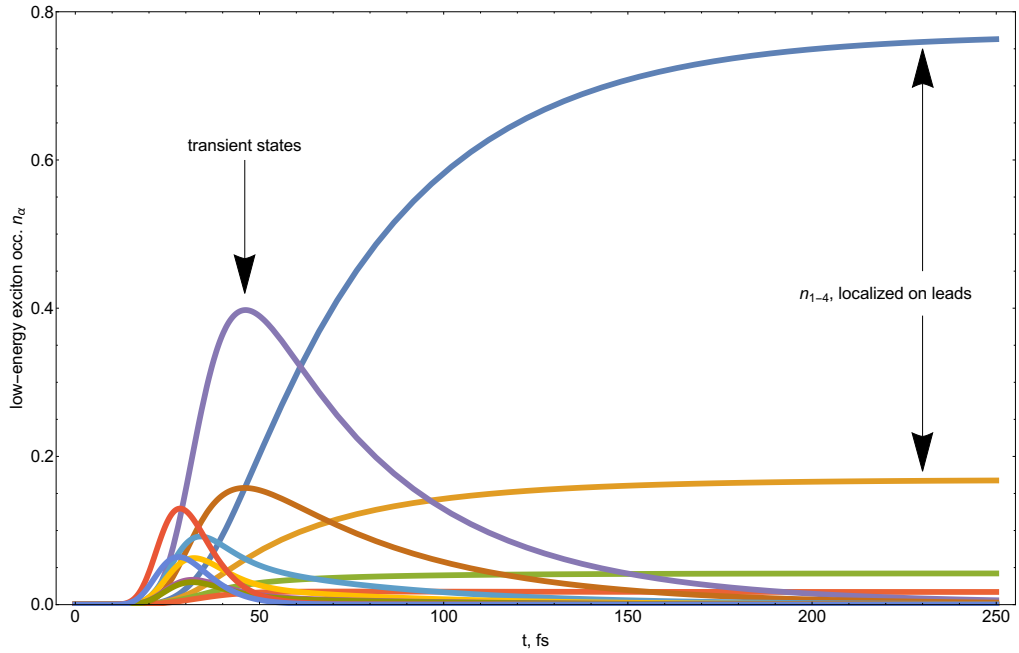

Figure 4.5. Solutions to the BE for $n_\alpha(t)$ for the smaller nanowire, for the 14 lowest energy exciton states α.

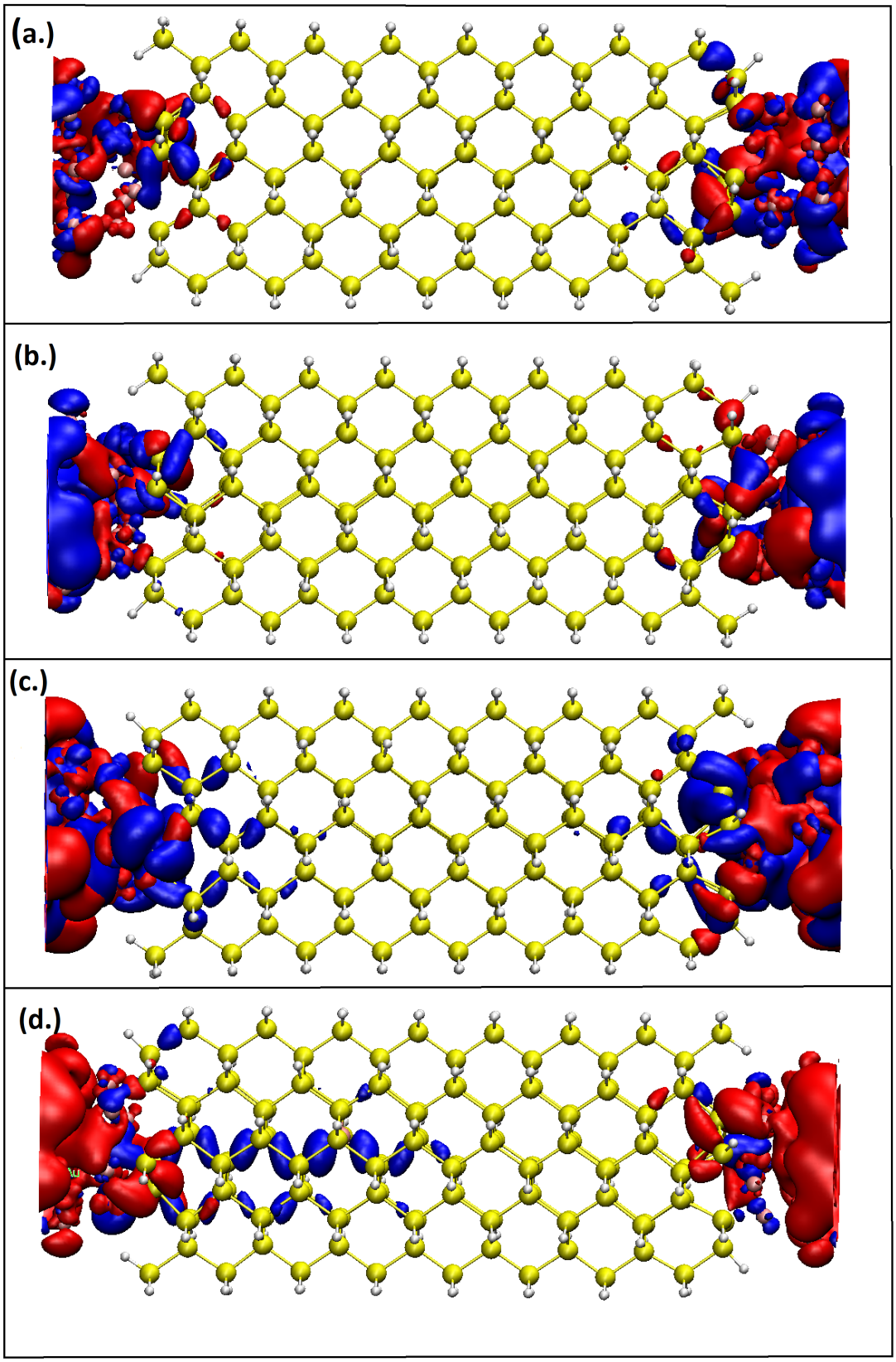

Figure 4.6. Visualization of orbitals on the smaller nanowire for the four lowest exciton states **(a.)** $\alpha = 1$ **(b.)** $\alpha = 2$ **(c.)** $\alpha = 3$ **(d.)** $\alpha = 4$. Holes are colored red and electrons are colored blue.

Given the solutions to the BE and the wave functions from the BSE, we can calculate the charge density

$$\begin{aligned}\rho(\vec{x},t) =& e\sum_{\alpha} n_{\alpha}(t)\sum_{eh} \mid \Psi^{\alpha}_{eh} \mid^2 (\mid \phi_e(\vec{x}) \mid^2 - \mid \phi_h(\vec{x}) \mid^2) \\ &+ e\sum_{\alpha\beta} n_{\alpha\beta}(t)\sum_{eh}(\mid \Psi^{\alpha}_{eh} \mid^2 + \mid \Psi^{\beta}_{eh} \mid^2)[\mid \phi_e(\vec{x}) \mid^2 - \mid \phi_h(\vec{x}) \mid^2],\end{aligned} \tag{4.1}$$

where the sum over eh is the expectation value of the charge density for an excitonic state α. Equation (4.1) weights the expectation value of the charge density of each state α by its corresponding occupation number, and adds it up for all included states. In this work, only the lowest 40 states are included, as they are the states that appreciably reside on the leads. The occupation numbers in equation (4.1) result from a solution to the BE from a particular excitation. We choose excitations corresponding to absorption peaks because those excitions should be delocalized throughout the silicon, as can be seen in Figure (4.7) which shows orbitals corresponding to the three absorption peaks for which we run simulate photoexcited state dynamics. See Figure (4.8) for a plot of the Projected Density of States (PDOS), which shows contributions from atom species to Kohn-Sham states. With the PDOS, we can see which excitons are likely to reside on different parts of the nanostructure, which gives us another way to find states to use for an initial excitation.

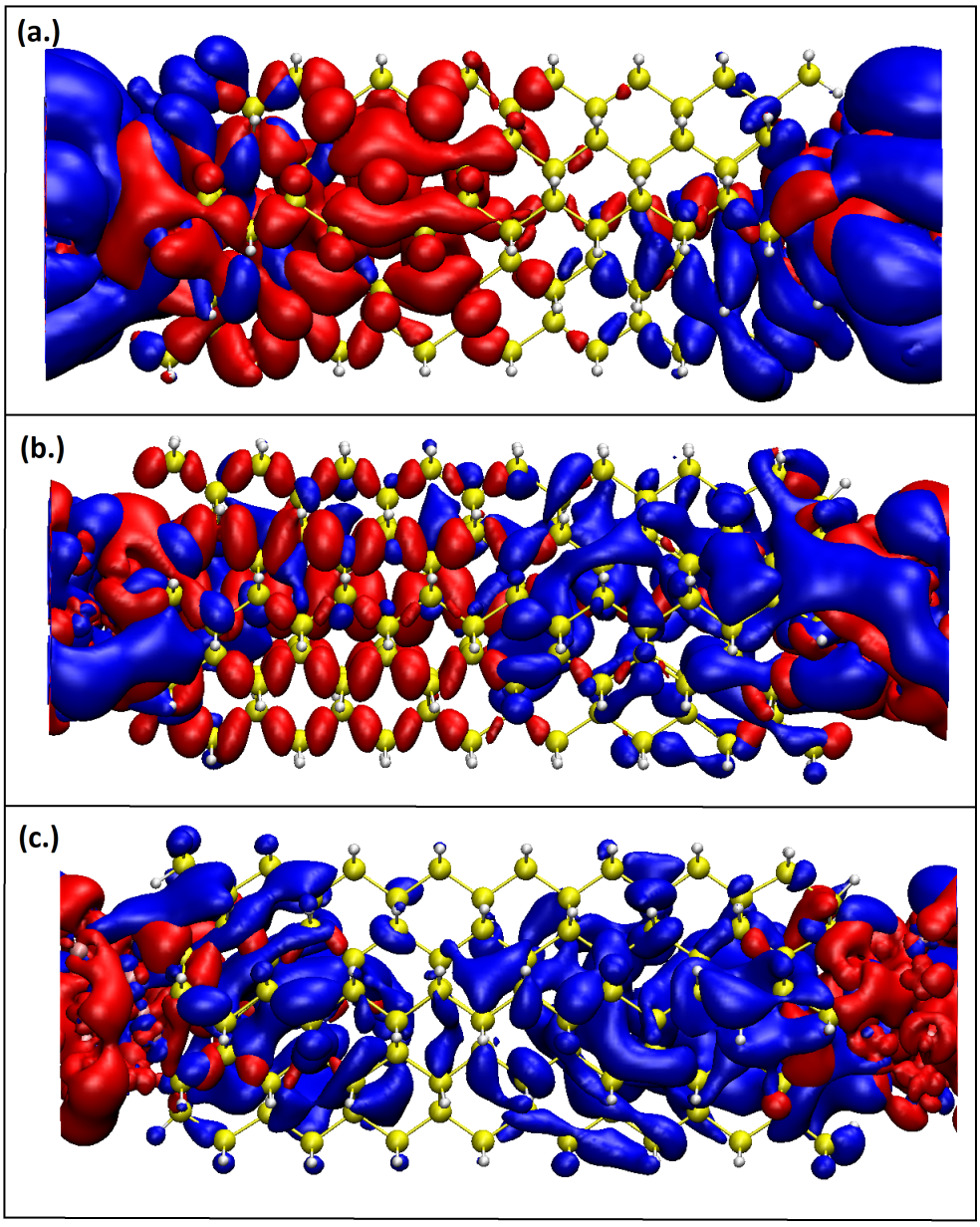

Figure 4.7. Orbitals for the excitons corresponding to absorption peaks at **(a.)** 1.7 eV, **(b.)** 2.2 eV, and **(c.)** 2.45 eV in the smaller nanowire.

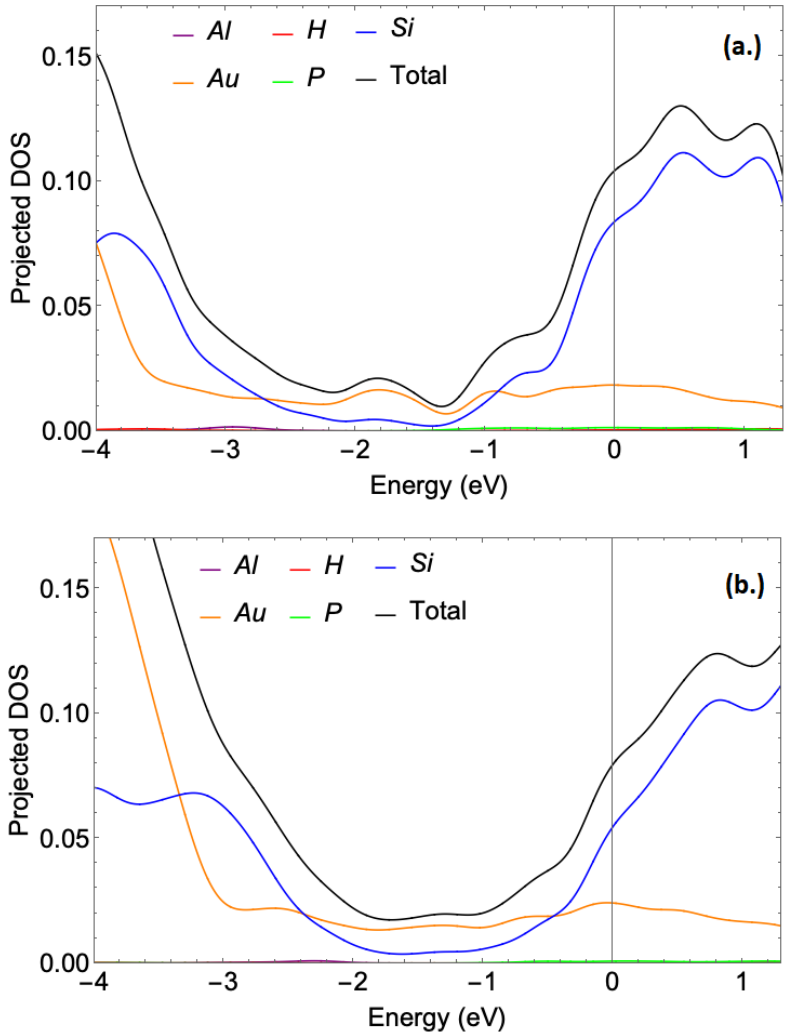

Figure 4.8. Projected Density of States (PDOS) shows the contributions to each Kohn-Sham eigenvalue of each atom species for **(a.)** the smaller nanowire with a HOMO at $-2.45\ eV$ and **(b.)** the larger nanowire with a HOMO at $-1.87\ eV$. Strictly speaking, each exciton is made up of a linear combination of Kohn-Sham states, but the fact that in both nanowires, eigenvalues near the HOMO are dominated by gold suggests that low-energy excitions are likely to reside on the leads. Likewise, the fact that eigenvalues far from the HOMO are dominated by silicon suggests that higher energy excitons are likely to reside on the silicon.

We then compute the density via equation (4.1) for each of the two leads(left and right), and integrate to get the charge

$$q_L(t) = \int_L d^3x \rho(\vec{x}, t), \qquad \text{and} \qquad q_R(t) = \int_R d^3x \rho(\vec{x}, t). \tag{4.2}$$

In equation (4.1), there are two terms with sums over eh. The first term sums over single exciton states α and the second sums over bi-exciton states α, β. Only keeping the first such term allows us to compute the charge without MEG, and keeping both allows up to compute the charge with MEG. Plotting both allows us to compare charge build up in the leads, and determine if there is enhancement in the charge due to MEG. This is shown in Figure (4.9) for one state per peak, which shows that we do see consistent enhancement of around 78%-79% across each of the three peaks. Realistically, each peak contains a range of states with similar energies, and Table (4.1) contains a list of enhancements for multiple states per peak.

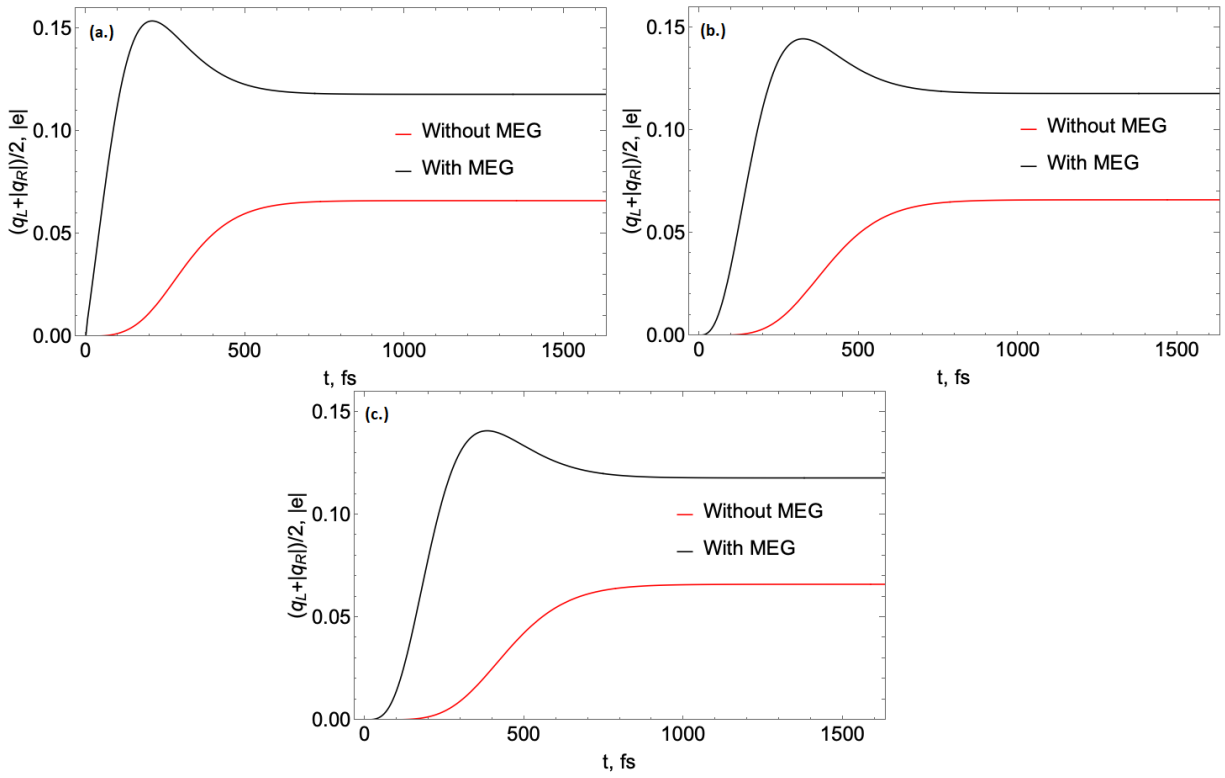

Figure 4.9. Plots of charge versus time in the smaller nanowire for initial excitations of **(a.)** 1.7 eV ($\alpha = 160$) **(b.)** 2.2 eV ($\alpha = 354$) **(c.)** 2.45 eV ($\alpha = 512$).

Table 4.1. A table of charge enhancement for a variety of states corresponding to three peaks at 1.7 eV, 2.2 eV, and 2.45 eV for the smaller nanowire.

Peak Energy	α	*Enhancement*	*Average*
$E = 1.7eV$	160	78.580%	78.581%
	161	78.580%	
	162	78.581%	
	163	78.582%	
	164	78.583%	
$E = 2.2eV$	354	78.890%	78.894%
	355	78.892%	
	356	78.895%	
	357	78.897%	
	358	78.896%	
$E = 2.45eV$	512	79.360%	79.372%
	513	79.364%	
	514	79.378%	
	515	79.380%	
	516	79.378%	

The charge curves for each of the peaks bear a striking resemblance, and their enhancements are also nearly equal. This is because the the solutions to the BE for each peak, while distinct, converge to nearly the same quasi-steady state value (See Figure A.1 in the Appendix).

4.5. Boltzmann Transport Equation and Charge Build-Up on the Leads in the Larger Nanowire

We now solve the BE for the thick wire, corresponding to an excitation at 1.25 eV. The orbitals of an exciton corresponding to this energy are shown in Figure (4.10). Refer back to Figure (4.8) for the PDOS. From this solution to the BE we can plot the 14 lowest energy exciton occupation numbers in a similar manner to what we did with the smaller nanowire, as can be seen in Figure (4.11). We see multiple excitons that reach a quasi-steady state, with only a few decaying into unoccupied states. The orbitals of four of the quasi-steady states, specifically those

of the four lowest energy states, can be seen in Figure (4.12) Using these occupancies, we can use equation (4.1) and (4.2) to compute the charge as a function of time. This is seen in Figure (4.13). The charge enhancement we see in the larger nanowire is 116%. Since we consider only bi-excition decay, whereby a charge carrier decays into two lower energy excitons, the most enhancement we should see is 100%. With this in mind, we only show results for the on absorption peak.

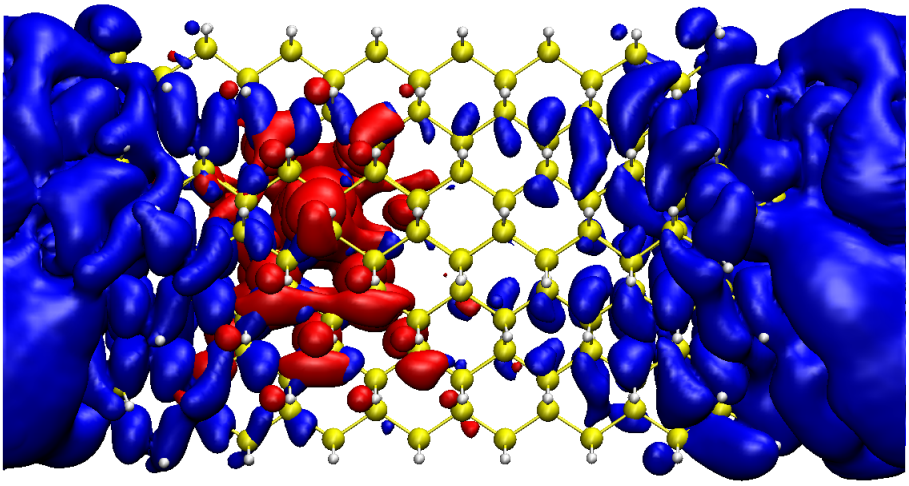

Figure 4.10. Orbitals of the exciton corresponding to an energy of 1.25 eV ($\alpha = 292$) in the thicker nanowire.

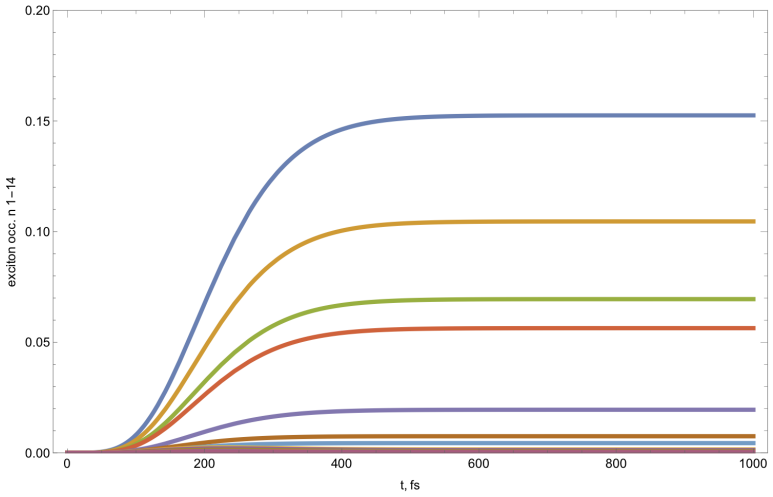

Figure 4.11. Solutions to the BE for $n_\alpha(t)$ for the thicker nanowire, for the 14 lowest energy exciton states α.

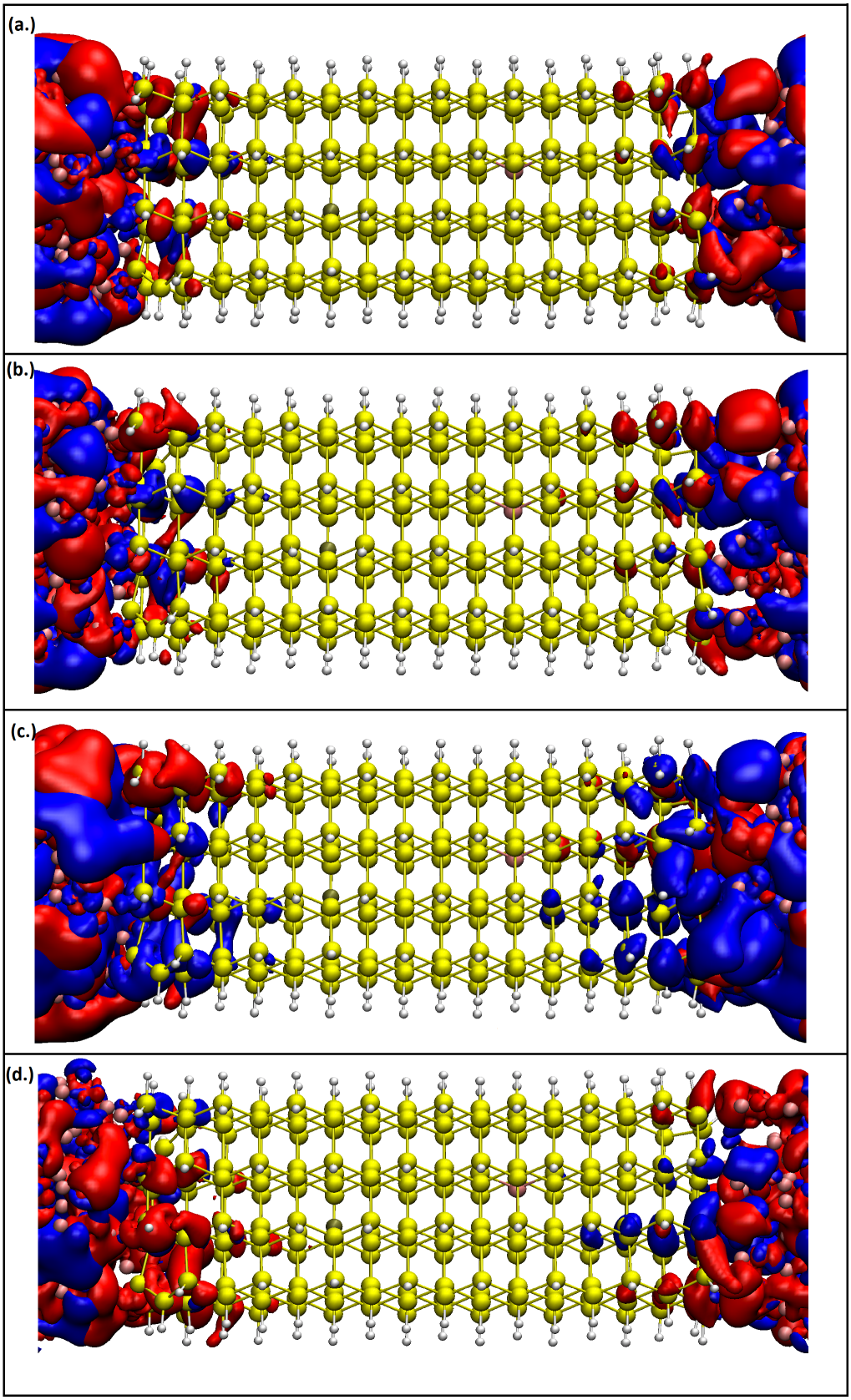

Figure 4.12. Visualization of orbitals on the larger nanowire for the states **(a.)** $\alpha = 1$ **(b.)** $\alpha = 2$ **(c.)** $\alpha = 3$ **(d.)** $\alpha = 4$. Holes are colored red and electrons are colored blue.

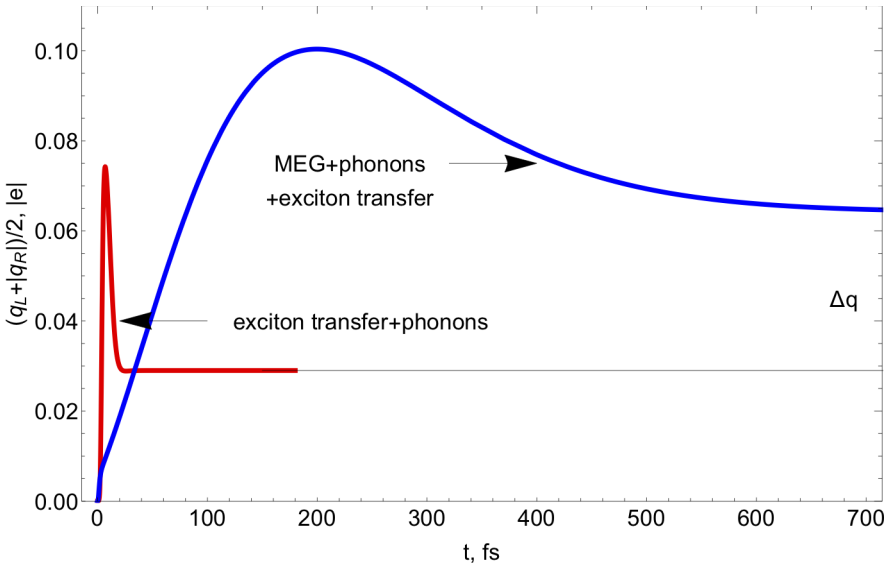

Figure 4.13. A plot of charge versus time, both with and without MEG, for an excitation corresponding to 1.25 eV in the thicker nanowire.

5. CONCLUSIONS AND OUTLOOK

In this work we modeled p-n junction photovoltaic devices with silicon nanowires of differing sizes, that have been doped with one Al atom and one P atom, and capped with gold leads. Due to the dopant atoms, both nanowires constitute a p-n junction with a built-in electric dipole. With these models, we simulated photo-excited state dynamics of charge-separated states. While we have results for the smaller nanowire, the results for a thicker nanowire are preliminary. By completing the results for the thicker nanowire, we will be able to test the confinement effect.

Starting with DFT simulations, we calculated optimized geometries of our systems, and their corresponding electronic structure. With the output from these calculations, we calculated phonon energies and solved the BSE. With these we were able to calculate rates of competing processes in a photoexcited state: phonon emission, MEG, and exciton transfer. Using these rates, we solved the BE for occupation numbers of different states from an initial photoexcitation. Using the occupation numbers, we calculated the charge buildup in the leads both with and without MEG processes. In particular, we found enhancement in charge due to MEG in both nanowires. However, the results for the thicker nanowire are preliminary, and work will be done in the future to finalize them.

There are a few ways the results of this project could be improved. One way would be to include a better treatment of the electronic structure. An implementation of the GW Method would allow us to improve the values of our single particle energies, in comparison to the results from the HSE06 Hybrid Functional.

The second way to improve this project would be to construct models that more accurately reflect real p-n junction photovoltaic devices. Most critically, due to the PBC in our models, we effectively have a short-circuit configuration in both of our models. Because of this, excitons effectively occupy the same space after time evolution. Exciton recombination is then more of an issue in our models than it would be in realistic photovoltaic devices. Making our models more realistic would require the inclusion of some modification which would effectively act as a resistor, and we would need to include a description of radiative and non-radiative exciton recombination. In addition, instead of using doped silicon nanowires which are 1D materials, it would be possible, and

more accurate, to use 2D materials as a model. The inclusion of either or both of these modifications would allow our results to have more impact on the development of solar technologies.

REFERENCES

[1] Andrei Kryjevski, Deyan Mihaylov, and Dmitri Kilin. Dynamics of Charge Transfer and Multiple Exciton Generation in the Doped Silicon Quantum Dot–Carbon Nanotube System: Density Functional Theory-Based Computation. *The Journal of Physical Chemistry Letters*, 9(19):5759–5764, October 2018.

[2] Andrei Kryjevski, Deyan Mihaylov, Svetlana Kilina, and Dmitri Kilin. Multiple exciton generation in chiral carbon nanotubes: Density functional theory based computation. *The Journal of Chemical Physics*, 147(15):154106, October 2017.

[3] Rolf E. Hummel. Semiconductor Devices. In *Electronic Properties of Materials*, pages 131–177. Springer, 4th edition, 2011.

[4] William Shockley and Hans J. Queisser. Detailed Balance Limit of Efficiency of p-n Junction Solar Cells. *Journal of Applied Physics*, 32(3):510–519, March 1961. Publisher: American Institute of Physics.

[5] Randy J. Ellingson, Matthew C. Beard, Justin C. Johnson, Pingrong Yu, Olga I. Micic, Arthur J. Nozik, Andrew Shabaev, and Alexander L. Efros. Highly efficient multiple exciton generation in colloidal PbSe and PbS quantum dots. *Nano Letters*, 5(5):865–871, May 2005.

[6] A. J. Nozik. Quantum dot solar cells. *Physica E Low-Dimensional Systems and Nanostructures*, 14:115–120, April 2002.

[7] J. Bude and K. Hess. Thresholds of impact ionization in semiconductors. *Journal of Applied Physics*, 72(8):3554–3561, October 1992. Publisher: American Institute of Physics.

[8] H. K. Jung, K. Taniguchi, and C. Hamaguchi. Impact ionization model for full band Monte Carlo simulation in GaAs. *Journal of Applied Physics*, 79(5):2473–2480, March 1996. Publisher: American Institute of Physics.

[9] D. Harrison, R. A. Abram, and S. Brand. Characteristics of impact ionization rates in direct and indirect gap semiconductors. *Journal of Applied Physics*, 85(12):8186–8192, May 1999. Publisher: American Institute of Physics.

[10] Arthur J Nozik. Spectroscopy and Hot Electron Relaxation Dynamics in Semiconductor Quantum Wells and Quantum Dots. *Annual Review of Physical Chemistry*, 52(1):193–231, 2001. _eprint: https://doi.org/10.1146/annurev.physchem.52.1.193.

[11] John A. McGuire, Milan Sykora, Jin Joo, Jeffrey M. Pietryga, and Victor I. Klimov. Apparent Versus True Carrier Multiplication Yields in Semiconductor Nanocrystals. *Nano Letters*, 10(6):2049–2057, June 2010. Publisher: American Chemical Society.

[12] Nathaniel M. Gabor. Impact Excitation and Electron–Hole Multiplication in Graphene and Carbon Nanotubes. *Accounts of Chemical Research*, 46(6):1348–1357, June 2013. Publisher: American Chemical Society.

[13] Kirill A. Velizhanin and Andrei Piryatinski. Numerical Study of Carrier Multiplication Pathways in Photoexcited Nanocrystal and Bulk Forms of PbSe. *Physical Review Letters*, 106(20):207401, May 2011. Publisher: American Physical Society.

[14] Kirill A. Velizhanin and Andrei Piryatinski. Numerical analysis of carrier multiplication mechanisms in nanocrystalline and bulk forms of PbSe and PbS. *Physical Review B*, 86(16):165319, October 2012. Publisher: American Physical Society.

[15] W. D. A. M. de Boer, E. M. L. D. de Jong, D. Timmerman, T. Gregorkiewicz, H. Zhang, W. J. Buma, A. N. Poddubny, A. A. Prokofiev, and I. N. Yassievich. Carrier dynamics in Si nanocrystals in an SiO${}_{2}$ matrix investigated by transient light absorption. *Physical Review B*, 88(15):155304, October 2013. Publisher: American Physical Society.

[16] John T. Stewart, Lazaro A. Padilha, Wan Ki Bae, Weon-Kyu Koh, Jeffrey M. Pietryga, and Victor I. Klimov. Carrier Multiplication in Quantum Dots within the Framework of Two Competing Energy Relaxation Mechanisms. *The Journal of Physical Chemistry Letters*, 4(12):2061–2068, June 2013. Publisher: American Chemical Society.

[17] G. Kresse and J. Furthmüller. Efficient iterative schemes for ab initio total-energy calculations using a plane-wave basis set. *Physical Review B*, 54(16):11169–11186, October 1996. Publisher: American Physical Society.

[18] G. Kresse and J. Furthmüller. Efficiency of ab-initio total energy calculations for metals and semiconductors using a plane-wave basis set. *Computational Materials Science*, 6(1):15–50, July 1996.

[19] G. Kresse and J. Hafner. Ab initio molecular-dynamics simulation of the liquid-metal–amorphous-semiconductor transition in germanium. *Physical Review B*, 49(20):14251–14269, May 1994. Publisher: American Physical Society.

[20] G. Kresse and J. Hafner. Ab initio molecular dynamics for liquid metals. *Physical Review B*, 47(1):558–561, January 1993. Publisher: American Physical Society.

[21] John P. Perdew, Kieron Burke, and Matthias Ernzerhof. Generalized Gradient Approximation Made Simple. *Physical Review Letters*, 77(18):3865–3868, October 1996. Publisher: American Physical Society.

[22] Jochen Heyd, Gustavo E. Scuseria, and Matthias Ernzerhof. Hybrid functionals based on a screened Coulomb potential. *The Journal of Chemical Physics*, 118(18):8207–8215, May 2003.

[23] Lars Hedin. New Method for Calculating the One-Particle Green's Function with Application to the Electron-Gas Problem. 1965.

[24] Lorin X. Benedict, Aaron Puzder, Andrew J. Williamson, Jeffrey C. Grossman, Giulia Galli, John E. Klepeis, Jean-Yves Raty, and O. Pankratov. Calculation of optical absorption spectra of hydrogenated Si clusters: Bethe-Salpeter equation versus time-dependent local-density approximation. *Physical Review B*, 68(8):085310, August 2003.

[25] Yulun Han, Sergei Tretiak, and Dmitri Kilin. Dynamics of charge transfer at Au/Si metal-semiconductor nano-interface. *Molecular Physics*, 112(3-4):474–484, February 2014. Publisher: Taylor & Francis _eprint: https://doi.org/10.1080/00268976.2013.842007.

[26] Yulun Han, David A. Micha, and Dmitri S. Kilin. Ab initio study of the photocurrent at the Au/Si metal–semiconductor nanointerface. *Molecular Physics*, 113(3-4):327–335, February 2015.

[27] Neil W. Ashcroft and N. David Mermin. *Solid State Physics*. Thomas Learning, 1976.

[28] Neil W. Ashcroft and N. David Mermin. The Semiclassical Model of Electron Dynamics. In *Solid State Physics*, pages 213–242. Thomas Learning, 1976.

[29] Neil W. Ashcroft and N. David Mermin. Inhomogeneous Semiconductors. In *Solid State Physics*, pages 589–614. Thomas Learning, 1976.

[30] Simone Pisana, Michele Lazzeri, Cinzia Casiraghi, Kostya S. Novoselov, A. K. Geim, Andrea C. Ferrari, and Francesco Mauri. Breakdown of the adiabatic Born–Oppenheimer approximation in graphene. *Nature Materials*, 6(3):198–201, March 2007. Number: 3 Publisher: Nature Publishing Group.

[31] M. Born and J. R. Oppenheimer. On the Quantum Theory of Molecules. 1927. Accepted: 2016-07-20T10:53:46Z.

[32] Neil W. Ashcroft and N. David Mermin. Beyond the Independent Electron Approximation. In *Solid State Physics*, pages 329–253. Thomas Learning.

[33] P. Hohenberg and W. Kohn. Inhomogeneous Electron Gas. *Physical Review*, 136(3B):B864–B871, November 1964. Publisher: American Physical Society.

[34] R. O. Jones and O. Gunnarsson. The density functional formalism, its applications and prospects. *Reviews of Modern Physics*, 61(3):689–746, July 1989. Publisher: American Physical Society.

[35] W. Kohn and L. J. Sham. Self-Consistent Equations Including Exchange and Correlation Effects. *Physical Review*, 140(4A):A1133–A1138, November 1965. Publisher: American Physical Society.

[36] Matthias Ernzerhof, John P. Perdew, and Kieron Burke. Coupling-constant dependence of atomization energies. *International Journal of Quantum Chemistry*, 64(3):285–

295, 1997. _eprint: https://onlinelibrary.wiley.com/doi/pdf/10.1002/%28SICI%291097-461X%281997%2964%3A3%3C285%3A%3AAID-QUA2%3E3.0.CO%3B2-S.

[37] Carlo Adamo and Vincenzo Barone. Toward reliable density functional methods without adjustable parameters: The PBE0 model. *The Journal of Chemical Physics*, 110(13):6158–6170, March 1999. Publisher: American Institute of Physics.

[38] Matthias Ernzerhof, Kieron Burke, and John P. Perdew. Long-range asymptotic behavior of ground-state wave functions, one-matrices, and pair densities. *The Journal of Chemical Physics*, 105(7):2798–2803, August 1996. Publisher: American Institute of Physics.

[39] At the Frontier of Particle Physics. volume 1, page 133. World Scientific, 2000.

[40] Catalin D. Spataru, Sohrab Ismail-Beigi, Lorin X. Benedict, and Steven G. Louie. Excitonic Effects and Optical Spectra of Single-Walled Carbon Nanotubes. *Physical Review Letters*, 92(7):077402, February 2004. Publisher: American Physical Society.

[41] Vasili Perebeinos, J. Tersoff, and Phaedon Avouris. Scaling of Excitons in Carbon Nanotubes. *Physical Review Letters*, 92(25):257402, June 2004. Publisher: American Physical Society.

[42] Catalin D. Spataru, Sohrab Ismail-Beigi, Rodrigo B. Capaz, and Steven G. Louie. Theory and Ab Initio Calculation of Radiative Lifetime of Excitons in Semiconducting Carbon Nanotubes. *Physical Review Letters*, 95(24):247402, December 2005. Publisher: American Physical Society.

[43] Michael Rohlfing and Steven G. Louie. Electron-hole excitations and optical spectra from first principles. *Physical Review B*, 62(8):4927–4944, August 2000. Publisher: American Physical Society.

[44] G. Strinati. Effects of dynamical screening on resonances at inner-shell thresholds in semiconductors. *Physical Review B*, 29(10):5718–5726, May 1984. Publisher: American Physical Society.

[45] J. Walecka A.L Fetter. *Quantum Theory of Many-Particle Systems*. McGraw-Hill, New York, 1971.

[46] Andrei Kryjevski, Brendan Gifford, Svetlana Kilina, and Dmitri Kilin. Theoretical predictions on efficiency of bi-exciton formation and dissociation in chiral carbon nanotubes. *The Journal of Chemical Physics*, 145(15):154112, October 2016.

APPENDIX

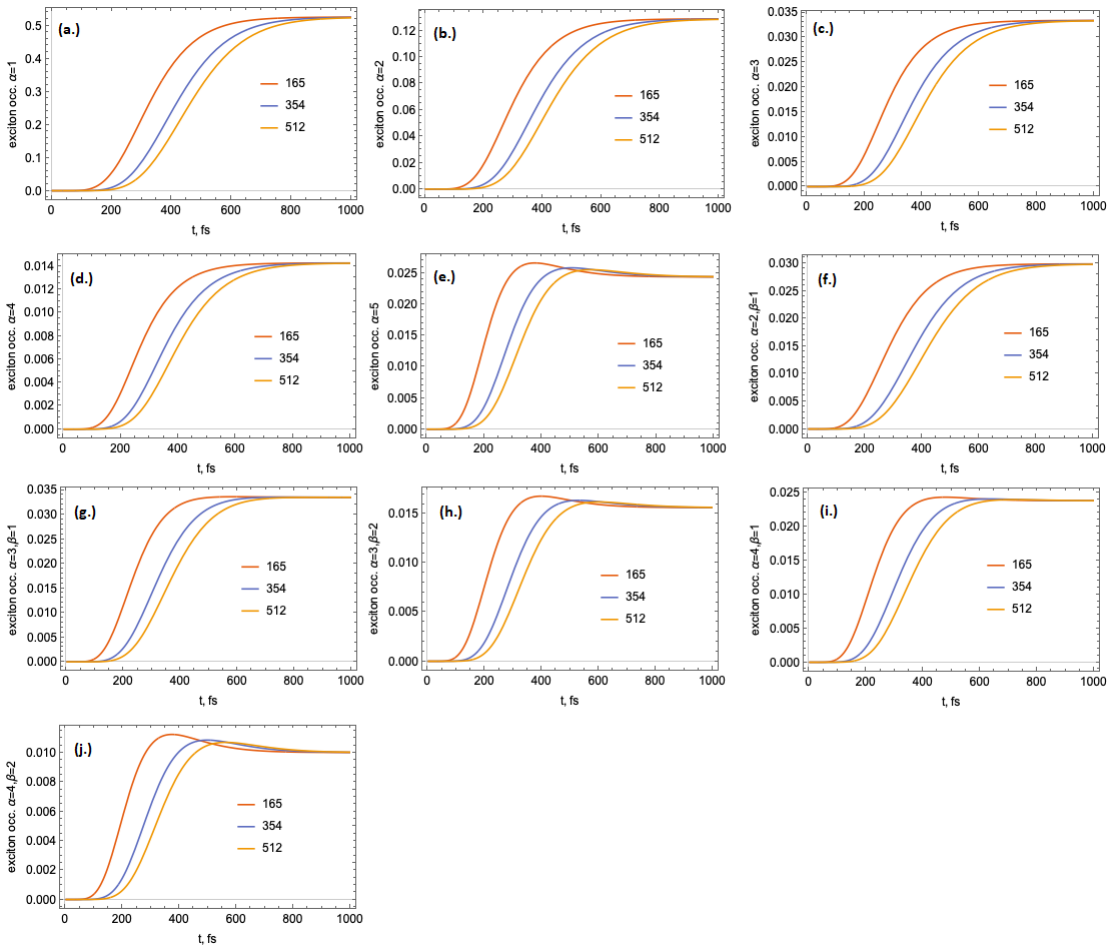

Figure A.1. Solutions to the BE for intitial exciton excitations corresponding to the absorption peaks 1.7, 2.2, and 2.45 eV, corresponding to exciton states $\alpha = 165$, 354, and 512, respectively. Each plot shows the occupation number of a given state for each of the three excitations. **(a.)-(e.)** show the five lowest energy single exciton states, while **(f.)-(j.)** show the five lowest energy bi-exciton states.